INVESTIGATION OF NONLINEAR OSCILLATIONS IN THE GAS DISCHARGE-SEMICONDUCTOR SYSTEM: EFFECT OF DIFFERENT FLUID MODELLING APPROACHES

A THESIS SUBMITTED TO
THE GRADUATE SCHOOL OF NATURAL AND APPLIED SCIENCES
OF
MIDDLE EAST TECHNICAL UNIVERSITY

CİHAN YEŞİL

IN PARTIAL FULFILLMENT OF THE REQUIREMENTS
FOR
THE DEGREE OF MASTER OF SCIENCE
IN
PHYSICS

JUNE 2018

Approval of the thesis:

INVESTIGATION OF NONLINEAR OSCILLATIONS IN THE GAS DISCHARGE-SEMICONDUCTOR SYSTEM: EFFECT OF DIFFERENT FLUID MODELLING APPROACHES

submitted by **CİHAN YEŞİL** in partial fulfillment of the requirements for the degree of **Master of Science in Physics Department, Middle East Technical University** by,

Prof. Dr. Halil Kalıpçılar
Dean, Graduate School of **Natural and Applied Sciences** ____________

Prof. Dr. Altuğ Özpineci
Head of Department, **Physics** ____________

Assoc. Prof. Dr. İsmail Rafatov
Supervisor, **Physics Department, METU** ____________

Examining Committee Members:

Assoc. Prof. Dr. Kemal Efe Eseller
Department of Electrical and Electronics Engineering,
Atılım University ____________

Assoc. Prof. Dr. İsmail Rafatov
Physics Department, METU ____________

Assoc. Prof. Dr. Hande Toffoli
Physics Department, METU ____________

Assoc. Prof. Dr. Burak Yedierler
Physics Department, METU ____________

Assoc. Prof. Dr. Alpan Bek
Physics Department, METU ____________

Date: ____________

I hereby declare that all information in this document has been obtained and presented in accordance with academic rules and ethical conduct. I also declare that, as required by these rules and conduct, I have fully cited and referenced all material and results that are not original to this work.

Name, Last Name: CİHAN YEŞİL

Signature :

ABSTRACT

INVESTIGATION OF NONLINEAR OSCILLATIONS IN THE GAS DISCHARGE-SEMICONDUCTOR SYSTEM: EFFECT OF DIFFERENT FLUID MODELLING APPROACHES

YEŞİL, CİHAN
M.S., Department of Physics
Supervisor : Assoc. Prof. Dr. İsmail Rafatov

June 2018, 76 pages

The work deals with the study of nonlinear oscillations in a system, consisted of planar glow discharge layer, coupled to a high-ohmic semiconductor layer. The whole system is sandwiched between two planar electrodes, to which the DC voltage is applied. The discharge models are developed in Comsol Multiphysics (v5.2), and based on fluid description of plasma, with drift-diffusion approximation for charged particle fluxes. Numerical tests are carried out for the discharge in Nitrogen, with GaAs semiconductor layer. We first derived and tested three different fluid models for DC glow discharge: the "simple" model, where the ionization is defined by the Townsend approximation, and two "extended" models with more detailed sets of plasma-chemical reactions. Accuracy and reliability of these models are analyzed by making comparison between the computed and experimental current-voltage characterics. Then, these models are applied to numerical investigation of the gas discharge-semiconductor system. First, the homogeneous stationary states of the system are identified. Then, the analysis of these states allows to develop bifurcation curves in the parameter space, separating the region where the plasma is stable from the region where it performs the homogeneous oscillations. Comparison with the experimental data allows to determine the accuracy and the ranges of applicability of different modelling approaches.

Keywords: Gas discharge, plasma, numerical modelling, nonlinear dynamics, phase transitions

ÖZ

GAZ BOŞALTIMI-YARI İLETKEN SİSTEMLERDE LİNEER OLMAYAN SALINIMLARIN ARAŞTIRILMASI: FARKLI AKIŞKAN MODELLERİN ETKİSİ

YEŞİL, CİHAN
Yüksek Lisans, Fizik Bölümü
Tez Yöneticisi : Doç. Dr. İsmail Rafatov

Haziran 2018 , 76 sayfa

Bu çalışmada yüksek dirençli yarı iletken tabakalar kullanımıyla oluşturulmuş parıltılı gaz boşaltımının lineer olmayan geçici salınımları incelenecektir. Bu sistem doğrusal akım uygulanmış iki tabaka arasında oluşturulmuştur. Gaz deşarjı olarak bilinen modeller Comsol Multiphysics (v5.2) yazılımıyla oluşturulmuş olup, plazmanın "drift-diffusion" yaklaşımının kullanımıyla akışkan olarak ele alınmasına dayanmaktadır. Nümerik testler GaAs malzemesinden yapılmış tabakalar arasında bulunan nitrojenin oluşturduğu basınçtaki gaz deşarjı fenomeni için yapılmaktadır. Bu çalışmada ilk önce üç farklı akışkan modeli oluşturulmuş ve kullanılabilirliği test edilmiştir. Bunlardan ilki ve yalın olanı için iyonizasyon mekanizması Townsend yaklaşımıyla tanımlanmış diğer iki modelse kimyasal reaksiyonları göz önünde bulundurarak daha detaylı hale getirilmiştir. Bu modellerin doğruluğu ve güvenilirliği akım-voltaj karakteristiklerinin deneysel sonuçlarla karşılaştırılmasıyla sağlanmıştır. Bu modeller sonrasında yarı iletkenli gaz deşarj sistemini tanımlamak için kullanılmıştır. Öncelikle bahsi geçen sistemin homojen kararlılık durumları belirlenip sonrasında bu durumların parametre uzayında incelemeleri yapılmıştır. Çıkan sonuçlar ışığı altında çatallanma gösteren eğrilerin (bu eğriler homojen salınımların ve kararlı plazma durumlarının belirlenmesinde kullanılır) ortaya çıkması sağlanır. Çıkan sonuçların deneysel verilerle kıyaslanması, yapılan yaklaşımların ne denli doğru ve kullanışlı olduğu hakkında bilgi edinilmesine yardımcı olur.

Anahtar Kelimeler: Gaz deşarj, plazma, nümerik modelleme, lineer olmayan dinamik sistemler, faz geçişleri

To my newborn niece Melike Uzuner

ACKNOWLEDGMENTS

I would first like to thank my thesis advisor Assoc. Prof. Dr. İsmail Rafatov. He has always helped me whenever I had a question about my research.
I would like to thank my family for providing me continuous encouragement throughout my life.
Finally, I would like to express my admiration to Fyodor Mihayloviç Dostoyevski, Leo Tolstoy, Franz Kafka, Mevlana Celaleddin Rumi, Jiddu Krishnamurti, Friedrich Nietzsche and Carl Gustav Jung. The books of them save me from sorrow and give me hope during tough times. I also want to share my personal motto from Paracelsus: "Alterius non sit, qui suus esse potest".

TABLE OF CONTENTS

CHAPTERS

LIST OF TABLES

TABLES

LIST OF FIGURES

FIGURES

LIST OF ABBREVIATIONS

LTP	Low Temperature Plasma
DC	Direct Current
RF	Radio Frequency
OES	Optical Emission Spectroscopy
AD	Aston Dark Space
NG	Negative Glow
PC	Positive Column
AD	Anode Dark Space
AG	Anode Glow
FD	Faraday Dark Space
ITO	Indium Tin Oxide
CCD	Charge Coupled Device
LFA	Local Field Approximation
LMEA	Local Mean Energy Approximation
MC	Monte Carlo
PIC	Particle in Cell
GDSS	Gas Discharge Semiconductor System
CVC	Current Voltage Characteristics
PDE	Partial Differential Equation
ODE	Ordinary Differential Equation
DAE	Differential Algebraic Equation
BDF	Backward Differential Formula

CHAPTER 1

INTRODUCTION

In the 1920s, the term "plasma" was first introduced by Irving Langmuir (1881-1957) to specify field free regions of ionized gas. [1]. It was usually considered to be the fourth state of matter beside solid, liquid and gas. Later, plasma was called the first state of the matter since it came before the other states of the matter in the history of the evolution of the Universe [2].

When a gas is heated up enough, the atoms or molecules collide with each other (elastically or inelastically) and knock out their electrons. As a consequence of escaping of electrons, a cloud of free electrons and ions is built up. As a result of this, a plasma including electrons, ions and neutral atoms is formed. The density of negatively charged particles are approximately equal to that of positively charged particles in a plasma medium (i.e. the overall charge of a plasma is roughly zero). This equality is called quasi-neutrality [3].

Plasmas are found in either of two types. First, natural plasma, such as lightining, aurorae, solar wind, ionosphere of the Earth, stars including the Sun, etc. Second, man-made plasma like noble gas lambs, fluorescent lights, fusion reactors, and plasma TVs. Plasma has important applications in many fields of research, technology and industry. For example, it is used in surface treatments such as coating, etching in microelectronics, in aerospace, automotive, steel, biomedical, and toxic waste management industries [4].

1.1 Classification of Plasmas

Plasmas can be classified in different ways as follows.

Temperature:

- Low temperature plasmas (T_e is less than 100 eV)
  E.g., arc plasma at normal pressure (thermal LTP), low pressure glow discharge (nonthermal LTP)
- High temperature plasmas (T_e is more than 100 eV)
  E.g., fusion plasmas, solar plasma

Here T_e is the electron temperature and LTP means "Low Temperature Plasma".

Thermodynamic equilibrium:

- Non-thermal or non-equilibrium plasmas ($T_e >> T_i \approx T_g$)
- Thermal or equilibrium plasmas ($T_e \approx T_i \approx T_g$)

T_i and T_g are ion and gas temperatures, respectively.

Pressure:

- Low-pressure plasmas ($p < 10\ Torr$)
- Moderate pressure plasmas ($10\ Torr < p < 100\ Torr$)
- High pressure plasmas ($p > 100\ Torr$)

Here p is the pressure of the medium.

Ionization degree:

- Weakly ionized plasmas ($\alpha = 10^{-6} - 10^{-1}$)
  E.g., aurora, gas discharge plasma
- Fully ionized plasmas (α is close to 1)
  E.g., fusion plasmas, solar plasma

$\alpha = n_i/(n_i + n_n)$ is called the degree of ionization, where n_i and n_n are ion and neutral number densities.
Frequency of applied voltage:

- DC discharge
- pulsed discharge (kHz)
- RF dicharge (MHz)
- Microwave discharge (GHz)

Magnetization:

- magnetic plasmas
- non-magnetic plasmas

Occurence of various sorts of plasma as function of plasma density and temperature is illustrated in Figure 1.1

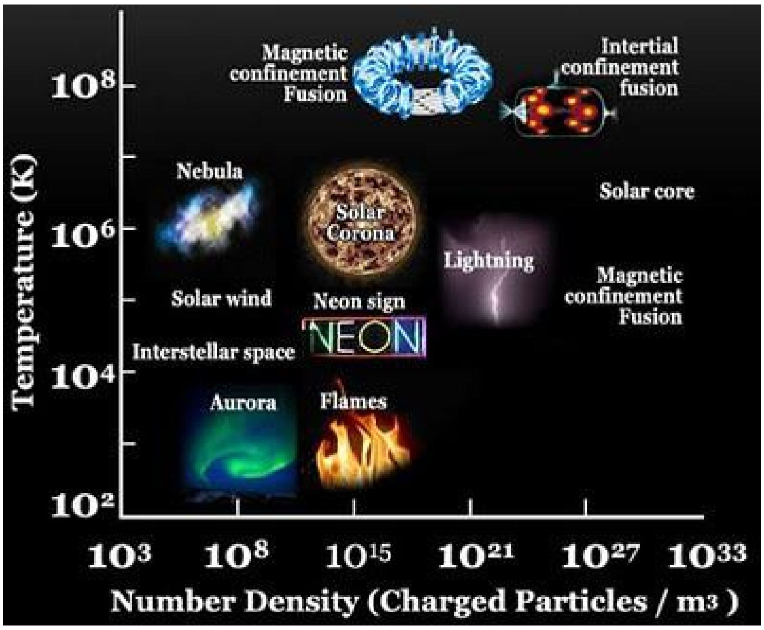

Figure 1.1: Classification of plasmas according to plasma density and electron temperature [5]

1.2 Regimes of DC discharge

Gas discharge is one of the ways to produce plasma. When the electric current flows through ionized gas inside a system comprising of two electrodes located in a closed vessel, then the electric discharge in gases occurs [6]. Current-voltage curves, luminescence, the current density and breakdown voltage are distinguishing characteristics of the discharges. These main characteristics depend on the geometry of the electrodes and the vessel, the type of the gas, and the electrode material. According to highly nonlinear current-voltage characteristics, the DC gas discharges are classified into three main types which are dark discharge, glow discharge and arc discharge as shown in Figure 1.2.

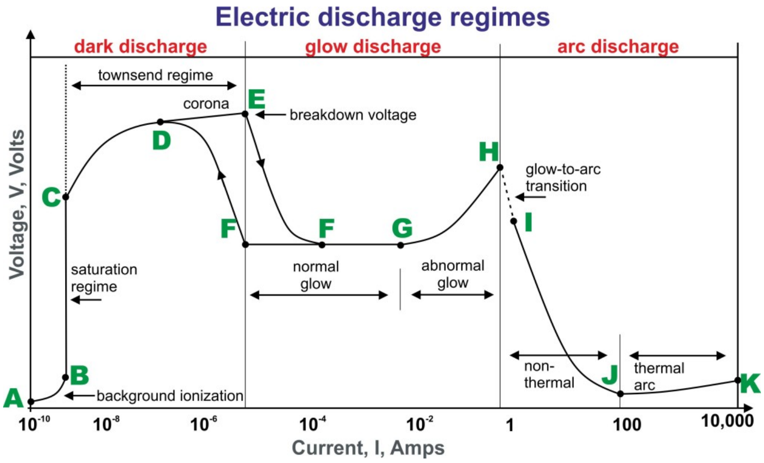

Figure 1.2: V/I plot of a DC gas discharge [7]

Dark Discharges : It is a regime occuring between the points A and E in the given figure. Except for corona region and the breakdown itself, the discharge is invisible to eye, so it is termed as a dark discharge.

In the background ionization stage, corresponding to the region between the points A and B, of the process, the density of charged particles is too low since they are created by the background radiation originating from cosmic rays, radioactive minerals, or other sources. Under the force of electric field, these charged particles move to the electrodes and produce a weak electric current. When the applied voltage is increased, more charged particles move to the electrodes, and current through the discharge increases. However, this is not enough to start an avalanche reaction inside the tube.

When the applied potential between the electrodes is increased, the system reaches to the saturation regime located between the points B and C. In this regime, all the available charged particles move to the electrodes and the current consequently saturates. Even if the applied voltage is increased, the current remains constant.

The regime occuring between the points C and E is called the Townsend discharge. As it seen from the Figure 1.2, when the applied voltage is increased across the discharge tube, the electric field becomes high enough for electrons to gain sufficient energy to ionize neutral atoms and hence creating more free charged particles. These newly secondary electrons themselves may also gain sufficient energy from the field to liberate futher electrons. In other words, each subsequent collision liberates another electron so that electron avalanche is realized in this way. Hence, the current increases with increasing of voltage.

In Townsend regime, the region between the points D and E corresponds to Corona discharge. This type of discharge occurs in regions of high electric field, typically at sharp points, edges, or wires in gases prior to electrical breakdown. Indeed, the strength of electric field plays a dominant role rather than the potential difference between the electrodes. Unlike the low currents where entire Corona is dark, Corona discharges look like a glow discharge when the Coronal currents are sufficiently high. Corona discharges only occupy the region of high electric field rather than the entire region between the electrodes, they are also called partial discharges, or "one-electrode discharges" since they show themselves around the only one electrode.

When the applied electric field is strong enough to develop electron avalanche process, the gas inside the tube will break down at the voltage V_b. Electrical break down is specified at the point E in Figure 1.2. For a specific gas and electrode material, the breakdown voltage depends on the product of pressure and the distance between electrodes. This dependency is expressed in Paschen's law [8]. It is an expression that describes the breakdown voltage as a function of pressure of the gas and gap length. It can be approximated by [4]

$$V_b = \frac{Bpd}{ln(Apd) - ln(ln(1 + 1/\gamma))} \tag{1.1}$$

Here γ is the secondary electron emission coefficient or second Townsend coefficient, p and d represent the pressure and gap length, A and B are experimentally determined electrode constants.

Glow Discharges : The name of this regime comes from glowing phenomenon of the plasma. When the energy and number density of the electrons are high enough to generate excited gas atoms during the collisions, the plasma gas emits light because excited electrons relax to their ground states.

As it is seen from Figure 1.2, the region between E and G is labelled as normal glow discharge. If it was followed by a discontinuous transition from E to F, the voltage across the discharge does not depend on total current density in this regime since only a small part of the cathode interacts with the plasma at the low currents. However, the occupied proportion of the cathode by the plasma is increased in the regime from F to G, where current increases. At the point G, the plasma interacts with the entire of the cathode surface. To move further away from point G, driving more current through the system is provided by increasing the applied voltage. In other words, the voltage is an increasing function of the current. The regime, located between G and H, is called abnormal glow regime. Unlike moving to the right from point G, a form of hysteresis in the current-voltage characteristic is observed by decreasing the current towards the point F, and the discharge maintains itself from F to F with making a transition back to the Townsend regime.

Arc Discharges : As it is stated before, it is the point H that cathode surface becomes sufficiently hot to thermionically emit electrons. When the supplied current is increased at the point H, the discharge undergoes a glow-to-arc transition as it is seen in Figure 1.2. It is also noted that the arc regime located between the points I and K is divided into two parts, thermal and non-thermal arc discharges. These two can be differentiated with respect to electrons being in thermal equilibrium with the gas medium. Arc discharges are widely used for welding, plasma cutting, and in spectrochemistry such as in Spark OES and DC arc spectroscopy.

1.3 Regions of glow discharge

Direct current glow discharge is sustained between two electrodes in a cell supplied with stationary voltage. When several hundred volts is applied through the electrodes, a fraction of atoms or molecules are initially ionized. Later, the positively and negatively charged particles are respectively driven towards cathode and anode by the electric field. During their journey, the collisions occur between the particles resulting in ionization, excitation, recombination, relaxation, dissocation etc. A bound electron in an atom is forced out of that atom in the ionization process. However, a less considerable transfer of energy to the bound electron would excite the electron to a higher energy level with a corresponding quantum absorption of energy. These excited states are unstable and electron comes back to its original state with the emission of a characteristic radiation. The glow of the glowing discharge is due to this mechanism. Moreover, the accelerated particles inside the gas medium strike the anode and cathode walls. One of the possible results of that is the emission of an electron. This physical process is called "secondary electron emission", and the number of ejected electrons per primary incident particles is also called "secondary electron coefficient" [9]. This phenomenon also plays a vital role in maintenance of the discharge. As a result of the factors mentioned above, main regions of the glow discharge can be illustrated in Crookes tube as shown Figure 1.3.

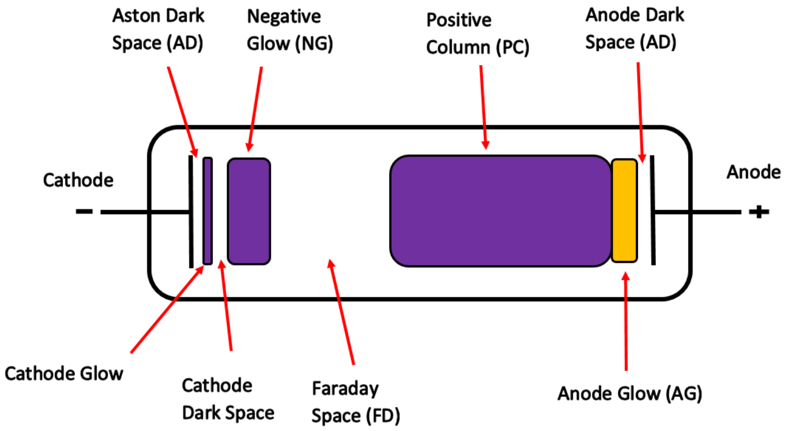

Figure 1.3: A Crookes tube illustrating the different regions inside a glow discharge

Aston Dark Space : This thin region is the closest one to the cathode. Electric field is strong enough to accelerate the electrons away from the cathode. Since the number of electrons is greater than that of ions, the space charge is negative. The reason why this region is dark is that the electron density and energy is not sufficient to excite the gas molecules and atoms.

Cathode Glow : It is a glowing region, so the energy of the electrons are high enough to excite the neutral gas atoms through the collisions. The axial extension of the region depends on the type of gas, the pressure and the temperature of the medium.

Cathode Dark Space : As the name suggests, it is a dark region. It has relatively high ion density. Positive ions move towards the cathode surface since the electric field is strong enough to accelerate them. When these ions hit the cathode surface, the emission of electrons occurs. These new electrons are also accelerated and cause the creation of new ions during collisions with neutrals in the Cathode Dark Space. The axial length depends on the applied voltage and the pressure of the medium. This region is also called "Cathode Fall".

Negative Flow : It is the brightest region of the discharge. Since there are high density of negative and positive charges, it is the region where most ionization and excitation processes take place. On the one hand electrons accelerated from cathode region are responsible for the ionizations, but on the other hand excitations, predominantly generating the negative glow are produced by slower electrons. Thus, the electrons at the end of the negative glow lose most of their energy in excitation and ionization processes. Although positive and negative charges are equal to each other in NG, the electric current is predominantly carried by the electrons due to having higher mobility.

Faraday Space : This dark region is found between the negative glow and positive column. Since electrons previously lose their most of the energy thorough the collisions in NG, their remaining energy is low in this region.

Positive Column : It is a luminous region and has a low net charge density. Although the electric field is small in the positive column, it is enough to ionize the gas with equal positive and negative charge densities. The length of the positive column depends on the geometry of the disharge tube. When the pressure increases, the positive column radially contracts. If the length of the tube is increased at constant pressure, the size of cathode regions do not change. The only change occurs in the length of the positive column. In contrast, the positive column region can be shortened to the negative glow region, so the positive column does not play a vital role in the operation of the discharge. The colour of glowing in this region depends on which type of gas is used.

Anode Glow : It occurs at the boundary of the anode sheath. Since the electric field gradient slightly increases towards the anode, the electrons passing in this region are accelerated and become more energetic. These electrons cause more emission of light near the anode than in the positive column. The AG region is thereby a bit brighter than the positive column.

Anode Dark Space : This region is located between the anode glow and anode surface. It is also called anode sheath. The region contains low energetic electrons to cause excitations because electrons have lost their energy during inelastic collisions in the AG region. The electric field is higher than in the positive column, so the electrons travel towards the anode. Because of this, Anode Dark Space has a negative space charge density.

1.4 Gas discharge modelling

Gas discharge plasmas are widely used in many industrial technologies and science. Understanding the fundamental physics of plasma processes is important to make progress in these fields. Experiments and numerical modellings of plasma are the ways to improve such an understanding. However, experimental investigations are not applicable in many situations because they can be expensive and labor consuming. Therefore, in these situations, numerical modelling approaches are more preferable than experimental approaches. Modelling of gas discharge is not an easy task since the number of particles is large and their interactions are complicated. Hence, following each particle individually is not possible. Instead of this, statistical descriptions are used by defining probability distribution function $f(\mathbf{r}, \mathbf{v}, t)$ for each species inside the discharge medium, and time evolution of this function is described by the Boltzmann equation [10]:

$$\frac{\partial f}{\partial t} + \mathbf{v} \cdot \nabla_{\mathbf{r}} f + \frac{\mathbf{F}}{m} \cdot \nabla_{\mathbf{v}} f = \left(\frac{\partial f}{\partial t} \right)_{coll.} \tag{1.2}$$

where m is the mass of the particle, $\nabla_{\mathbf{r}}$ and $\nabla_{\mathbf{v}}$ stands for the gradient in coordinate and velocity spaces, respectively, $\mathbf{F}$ is the applied electromagnetic force, and $\left(\frac{\partial f}{\partial t}\right)_{coll.}$ is the time rate of change of f due to collisions. Analytical solutions of this equation are possible but only for idealized models and a limited range of conditions [11]. The numerical modelling approaches are also developed and categorized as fluid models, kinetic (particle) models and hybrid models.

Fluid models are developed from moments of the Boltzmann equation. The moments are obtained by multiplying the Boltzman equation with powers of velocity and integrating over velocity space. The first three moments of the Boltzmann equation are responsible for particle, momentum and energy conservations, respectively. In addition to this, drift-diffusion approximation for fluxes is made to further simplify these reduced set of equations.

Fluid models can be collected under two headings, "simple fluid approach" and "extended fluid approach". First of them only uses first two moments of the Boltzmann equation. Transport and rate coefficients for this approach depend on the local value of the reduced electric field. This assumption is called as local field approximation (LFA). To improve accuracy of simple fluid model, extended fluid model is developed by incorporating the electron energy balance equation to define transport and rate coefficients as functions of local mean energy. This is called local mean energy approximation (LMEA). Physical results from extended fluid approach show qualitative agreement with results of direct solution of Boltzmann equation [12]. Because of this, LMEA is more recommended than LFA in fluid models.

The advantage of fluid models is efficiency in terms of computational speed; therefore, these models are applicable to make geometrically complex, higher dimensional analyses and calculations including complicated chemistry. However, the disadvantage of fluid models is not providing high accuracy due to not treating the particles at the kinetic level. For example, fluid model cannot capture nonlocal transport of electrons in all extents, so they are more preferable for high pressure discharges in which nonlocal effects are not so important.

Kinetic (particle) models track plasma particles individually under the influence of fundamental laws (Newton-Lorentz equation and Maxwell equations). This allows particle models to capture kinetic and nonlocal effects unlike fluid models. Since individual tracking of each particle is computationally impossible, particle-in-cell model uses 'superparticles', a group of real particles. Each superparticle typically corresponds to 10^5-10^7 real particles, and fundamental physics does not change because of collective behaviour of plasmas. In order to update position and velocity of each particle, motion of superparticles is found by integrating the Newton-Lorentz equation of motion. The necessary forces are calculated by interpolating field values specified at grid points to the position of each particle. The field values at the grid points are determined by using the Maxwell equations. The collisions between particles and with the electrode surfaces are calculated by using Monte-Carlo (MC) method. Indeed, PIC technique is complemented with MC method for collision processes. This fully kinetic simulation technique is called as PIC/MC method.

The particle models give physically more accurate results than fluid models since particle models follow superparticles individually. However, tracking of individual particles leads to computational cost. Thus, kinetic (particle) models are suitable for low pressure discharges with simple geometry and chemistry since there are a limited number of species under which nonlocal effects are important.

Hybrid model represents a compromise between efficiency of fluid models and accuracy of kinetic models. The positive ions and bulk electrons are modelled with the help of fluid methods whereas fast electrons are treated with in the frame of kinetic (particle) models. Since fast electrons have large energies leading to inelastic collisions, they are not in equilibrium with plasma medium. Therefore, the nonlocal character of transport and rate coefficients are captured by treating fast electrons with kinetic methods (such as MC simulation) for the sake of accuracy. However, the roles of the slow electrons are to carry electrical current and to form negative space charge. Because of this, bulk electrons and heavy ions are treated as continuum by describing them in a fluid approach for the sake of efficiency.

Hybrid models do not work self-consistently because fluid and kinetic (particle) methods have typically different time scales to make calculations. However, this method is a useful tool to describe a wide range of discharge physics phenomena due to its flexibility and exploiting the advantages of two methods, i.e. computational time of the fluid method and kinetic accuracy of the particle method.

Figure 1.4 illustrates a diagram, which gives an insight about choosing a correct physical model for a plasma system. Models are stated as functions of system size and pressure.

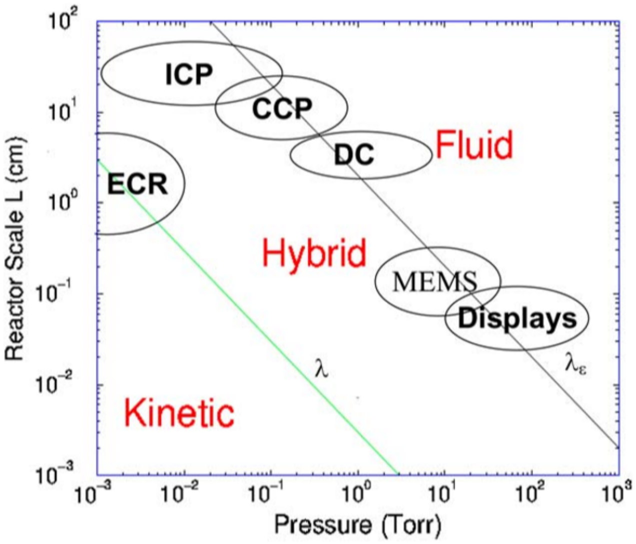

Figure 1.4: A diagram illustrating a correct physical model for a plasma system as functions of system size and pressure [13]

1.5 Pattern formation in gas discharge plasma

The understanding of pattern formation in nonlinear systems is among the most challenging topics in modern research. Pattern formation is a process including sequences of events. These events occur in a self-organized manner, so the pattern formation and self-organization are perceived as a single phenomenon in the literature [14]. Variety types of pattern formation and self-organization can be observed in both natural and technological contexts such as biological, chemical and physical systems [15]. In particular, plasma planar systems with high ohmic barrier can be taken as an example, which is schematically illustrated in Figure 1.5. The investigations for this gas discharge-semiconductor system (GDSS) are mainly carried out by the group of Purwins (Munster, Germany) and by the group of Astrov (St.Petersburg, Russia). It has been found that this system shows a rich variety of patterns.

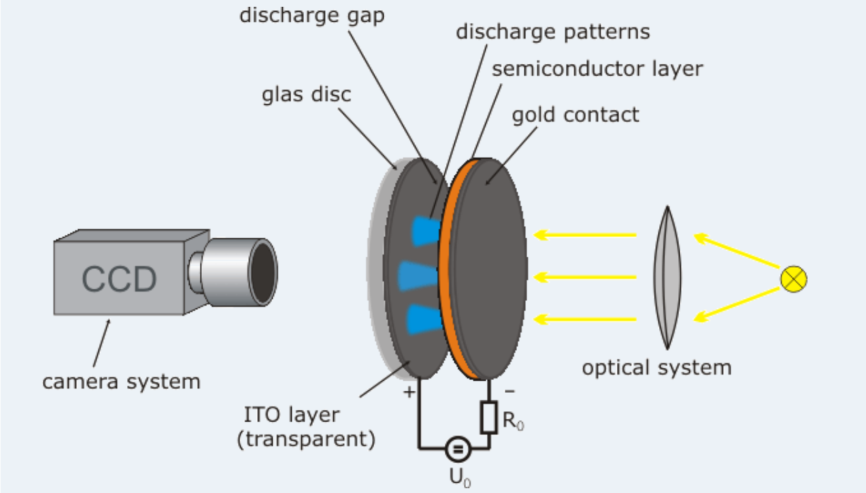

Figure 1.5: Planar DC gas discharge system with high ohmic cathode [16]

Unlike usual long discharge tubes, this experimental setup has a small aspect ratio, the ratio of width to height, and a high ohmic semiconductor cathode. As it is seen, the discharge gap is a sandwich like structure. The planar electrode at the anode side is made from a transparent indium tin oxide (ITO layer) deposited on a glass disc since the anode does not prevent the camera system from recording. However, planar electrode at the cathode side consists of semiconductor layer (such as GaAs) and gold material. Optical system is designed to make the camera visualisation possible. The system is supplied by a DC voltage source, and overall view of the pattern formation processes are recorded by a CCD (charge coupled device) camera system through the transparent electrode.

When sufficient current is supplied to the system, spatially and temporally inhomogeneous patterns (called as spatiotemporal patterns) are observed in the lateral direction perpendicular to the direction of the current in the discharge. The luminescence radiation from the discharge gap plays a key role to visualize the patterns. This radiation property is also proportional to the current density in the gap so that one can establish a relation between observed luminance density distribution and current density distribution in the gas.

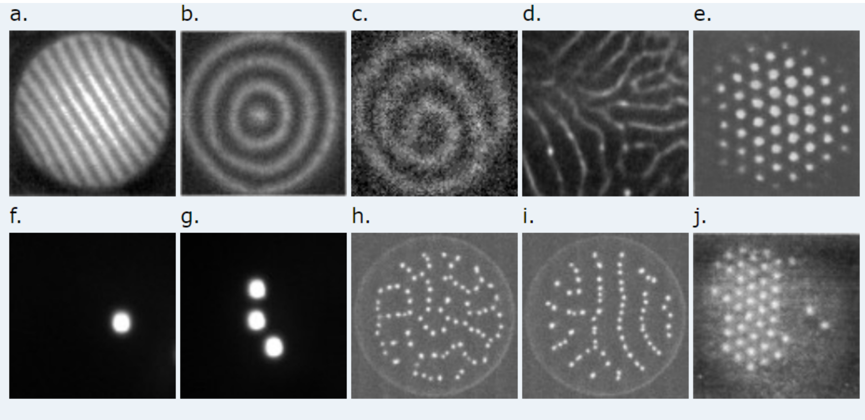

Figure 1.6: Some of the experimentally observed patterns [16]

Some of the experimentally observed structures are taken from the reference [16] and shown in the Figure 1.6. Figure (1.6-a), (1.6-b), (1.6-c), (1.6-d) and (1.6-e) demonstrates to stripe pattern, target pattern, spiral, labyrinth pattern, hexagonal pattern, respectively. It is noted that Figure (1.6-f) only consists of localized bright spot. It means that the pattern is not easily affected or disturbed by the fluctuations in the system. Because of this, the structure shows particle like properties and thereby is called as dissipative solitons [17]. Dissipative solitons do not only show isolated structures but also come together and interact with each other by showing particle properties to construct complex structures; for instance, molecules formation in Figure (1.6-g), nets in Figure (1.6-h), chains in Figure (1.6-i), and combination of different phases in one domain in Figure (1.6-j). The structures may also include chaotic behavior as in [18], [19].

In addition to above structures, the GDSS systems have homogeneous stationary and oscillating modes. For example, the state of homogeneous oscillations for a GDSS filled with nitrogen gas has been experimentally revealed in [20]. A representative example for homogeneous current oscillations are illustrated in Figure 1.7. Later, in [19], the oscillations with different frequencies for the same system has been observed, and the current oscillations with different frequencies are shown in Figure 1.8.

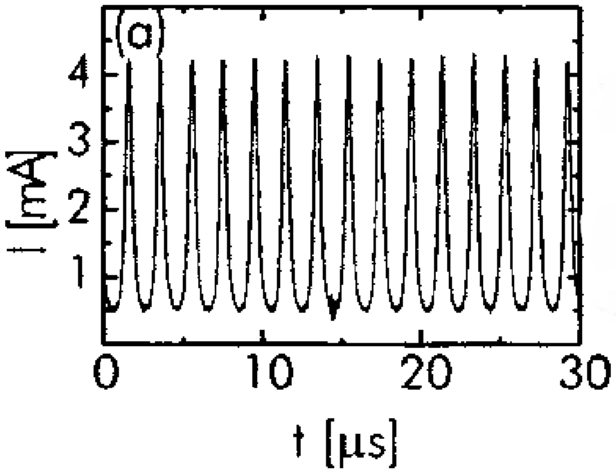

Figure 1.7: The discharge current I for the state of homogeneous oscillation [19]

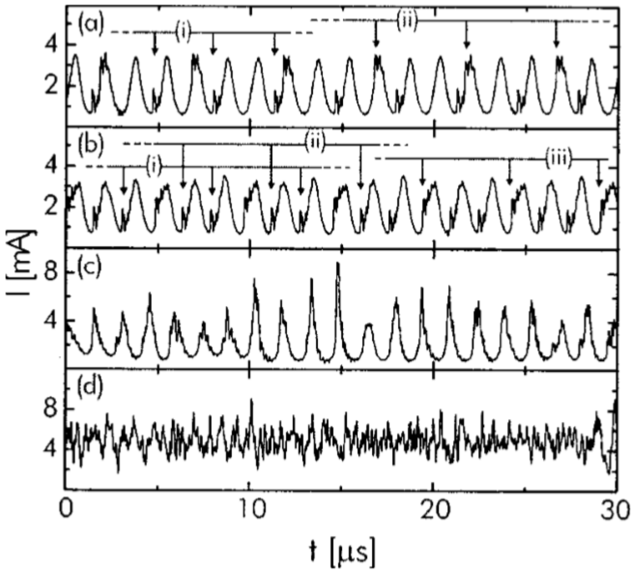

Figure 1.8: The discharge current I oscillations with different frequencies [19]

In the work [21], the focus is temporal oscillations of the physical parameters such as current and voltage instead of pattern formation. The reason is that transverse directions of the GDSS are considered spatially homogeneous; therefore, the only spatial changes occur in the direction perpendicular to the electrodes. This study is important for this thesis since the same parametric regimes are considered, and the developed models are more advanced forms of the model used in this study.

1.6 Aims and Motivations

In this thesis, three one dimensional discharge models for nitrogen gas are developed by using COMSOL Multiphysics software [22]. Plasma fluid equations are coupled with Maxwell equations to have a self-consistent model. Unlike Model-1 constructed with "simple fluid approach", Model-2 and Model-3 are created with "extended fluid approach". However, Model-2 and Model-3 differentiate from one another in the set of reactions they include. Since Model-3 includes more detailed plasma-chemical mode than Model-2, it is expected that the results from Model-3 must reflect the physical reality better than Model-2 and Model-1.

In order to test applicability of these three models, verification of the models are made for DC glow discharge conditions of N_2 by comparing their CVC (current-voltage characteristics) curves with the experimental CVC's available from literature [23], [24], [25], and [26]. This comparison is made for two purposes. One of them is to show applicability of the models for later analysis. The other one is to test whether CVC curve from Model-3 gives the best result or not. Spatial distributions of basic plasma parameters for each model are investigated and compared with each other to ensure that behaviours for each model show the same qualitative features at the three typical regimes: abnormal, normal, and subnormal.

After verification of the developed models, semiconductor layer is added at the cathode of the models to observe destabilization of stationary solutions in the regime between Townsend and normal glow. The control parameters are specified in terms of conductivity of the semiconductor and applied voltage. The resulting bifurcation curves for each of the models are compared with experimental data [27], [28], [21] in order to understand which model is most successful to reflect the physical reality.

The main purpose of the study is to understand the temporal oscillations of the plasma parameters although the discharge system is one dimensional and fed by a DC voltage source. This is important because understanding of purely temporal oscillations in spatially homogeneous mode is a first systematic step to predict the variety of spatiotemporal patterns.

1.6.1 Organization of the thesis

In Chapter 2, the fluid equations are developed from the moments of the Boltzmann equations with drift-diffusion approximation for fluxes. They are also coupled with Maxwell equations to obtain a self-consistent model. "simple fluid model" and "extended fluid model" are introduced with corresponding approximations: "local-field-approximation" (LFA) and "local-mean-energy-approximation" (LMEA). Plasma chemical reactions, transport coefficients, source terms, and boundary conditions are introduced, corresponding to three considered models. COMSOL Multiphysics software is finally introduced with the details of the calculations. Chapter 3 describes comparison of the models and their applicability. Firstly, parameter regimes for three considered models are specified. Later, CVC curves from the considered models are verified by comparing them with experimental and computed CVC curves taken from the literature. Spatial distributions of basic plasma parameters for three models are investigated for three different regimes of CVC diagram: abnormal, normal, and subnormal. In Chapter 4, a system consisted of a planar gas discharge coupled with a semiconductor layer between electrodes is introduced; parameter regime is described and dimensionless forms of physical parameters are derived. For a specific value of semiconductor resistance, the destabilization of stationary solutions for each model is determined by changing the control parameter. Besides, the corresponding bifurcation curves for three considered models are plotted and compared with experimental data. Finally, the conclusion is presented.

CHAPTER 2

MODELS

In this chapter, two-fluid equations of plasma are derived by evaluating the moments of the Boltzmann equation. Then, these equations are reduced to the model with drift-diffusion approximation for fluxes. In addition, Poisson equation is added to have a self-consistent model. After defining governing equations of the plasma fluid theory, "simple" and "extended" fluid models are defined and compared in terms of which fundamental needs they meet or not, with the aim to determine which one of them is more preferable than other. Unlike Model-1 constructed with "simple fluid approach", Model-2 and Model-3 are developed with "extended fluid approach". Moreover, plasma chemical reactions, transport coefficients, source terms and boundary conditions are described for these three considered one-dimensional models. Finally, COMSOL Multiphysics software, the development tool for these three models, are introduced, and some details for the calculations are given.

2.1 Governing Equations

The description of plasma can be made by using a probability distribution function $f(\mathbf{r}, \mathbf{v}, t)$. It describes the probability of finding the plasma particles at a given position, at a given velocity and at a given time in six-dimensional $(\mathbf{r}, \mathbf{v})$ space [1]. According to kinetic theory, the Boltzmann equation can be used to establish the shape of the probability distribution function under the effect of external forces. However, solving the Boltzmann equation directly is not an easy task. Fortunately, the integrations of the particle distribution function are equivalent to the macroscopic quantities (e.g. number density of the particles, mean velocity, etc) of the plasma. Therefore, taking the moments of the Boltzmann equation is an applicable way instead of direct solving the Boltzmann equation for the probability distribution function. The equations from the moments of the Boltzmann equation with the Maxwell equations form the foundation of the plasma fluid theory.

When force is specified as Lorentz force, the Boltzmann equation for one species of particles is as follows

$$\frac{\partial f}{\partial t} + \mathbf{v} \cdot \nabla_{\mathbf{r}} f + \frac{q}{m}(\mathbf{E} + \mathbf{v} \times \mathbf{B}) \cdot \frac{\partial f}{\partial \mathbf{v}} = \left(\frac{\partial f}{\partial t}\right)_{coll.} \tag{2.1}$$

where m is the mass of the particle, q is the charge of the particle, $\mathbf{E}$ is the electric field, $\mathbf{B}$ is the magnetic field, $\nabla_{\mathbf{r}}$ and $\frac{\partial f}{\partial \mathbf{v}}$ stands for the gradient in coordinate and velocity spaces, respectively. The term in the right hand side represents the time rate of change of f due to collisions. Moreover, the left hand side of the equation is actually equal to total time derivative of the probability distribution function $\frac{\mathrm{d}f}{\mathrm{d}t}$, so this equation simply says that this function does not change with time unless there are collisions between the particles [29].

2.1.1 Moments of the Boltzmann Equation

As it is mentioned before, the fluid equations are the moments of the Boltzmann equation. To implement that both sides of the equation (2.1) must be multiplied by powers of the velocity vector $\mathbf{v}$ and integrated over velocity space.

The zeroth-order moment : Both sides of the equation (2.1) are multiplied with $v^0 = 1$ and integrated over velocity space as it is seen below

$$\begin{aligned} &\int \frac{\partial f}{\partial t} d\mathbf{v} + \int (\mathbf{v} \cdot \nabla_{\mathbf{r}}) f d\mathbf{v} \\ +\frac{q}{m} \int [(\mathbf{E} + \mathbf{v} \times \mathbf{B}) \cdot \nabla_{\mathbf{v}}] f d\mathbf{v} &= \int \left(\frac{\partial f}{\partial t}\right)_{coll.} d\mathbf{v}. \end{aligned} \tag{2.2}$$

Using vector identities and carrying out some mathematical operations, expression (2.2) is reduced to [1]

$$\frac{\partial n}{\partial t} + \nabla_{\mathbf{r}} \cdot (n\mathbf{u}) = 0 \tag{2.3}$$

where n is the particle number density and $\mathbf{u}$ is the average velocity, defined as fluid velocity. The integral expressions including probability distribution functions for these two quantites are

$$n(\mathbf{r},t) = \int f(\mathbf{r},\mathbf{v},t)d\mathbf{v} \tag{2.4}$$

and

$$u(\mathbf{r},t) = \frac{1}{n(\mathbf{r},t)} \int \mathbf{v} f(\mathbf{r},\mathbf{v},t)d\mathbf{v}. \tag{2.5}$$

Equation (2.3) is a continuity equation. In this case, it accounts for conservation of charge and mass [1]. Equations describing conservation of these two quantites can be obtained by multiplying the equation with q and m, respectively. Moreoever, first term of (2.3) symbolizes the rate of particle change within the volume unlike the second term representing the flow of particles out of the volume. It is noticed that these two terms of the continuity equation must balance each other when particles are neither created nor destroyed. Otherwise, a source term representing the creation and destruction phenomenon is needed in the right hand side of (2.3).

The first-order moment : When the equation (2.1) is multiplied with mv and integrated over velocity space, the Boltzmann equation becomes

$$\begin{aligned} &m\int \mathbf{v}\frac{\partial f}{\partial t}d\mathbf{v} + m\int \mathbf{v}(\mathbf{v}\cdot\nabla_{\mathbf{r}})f d\mathbf{v} \\ +q\int \mathbf{v}[(\mathbf{E}+\mathbf{v}\times\mathbf{B})\cdot\nabla_{\mathbf{v}}]f d\mathbf{v} &= \int m\mathbf{v}\left(\frac{\partial f}{\partial t}\right)_{coll.} d\mathbf{v}. \end{aligned} \tag{2.6}$$

Then, the first-order moment of the Boltzmann equation is obtained as follows [1]

$$mn\frac{\mathrm{d}\mathbf{u}}{\mathrm{d}t} = -\nabla_{\mathbf{r}}\cdot\mathbf{\Psi} + qn(\mathbf{E}+\mathbf{u}\times\mathbf{B}) + \mathbf{S}_{ij} \tag{2.7}$$

where $\mathbf{S}_{ij} = \int m\mathbf{v}\left(\frac{\partial f}{\partial t}\right)_{coll} d\mathbf{v}$. As it is seen above, two new parameters are introduced. The first of them is pressure tensor, $\mathbf{\Psi}$. The diagonal terms of this tensor (e.g. p_{xx}, p_{yy}, etc.) represents the normal pressure. For instance, p_{xx} is the force per unit area applied on a plane surface normal to the x direction. However, the off-diagonal terms represent the shearing stresses. For example, p_{yx} is the force per unit area in the x direction, but it is applied on a plane surface perpendicular to y direction. The term $\mathbf{S}_{ij}$ is responsible for the rate of change of momentum density due to collisions between different species.

In principle, this equation is an expression for the conservation of momentum. The term in the left hand side is in the form of mass times acceleration, and the right hand side terms represent forces arising from pressure gradient, the Lorentz force and collisions, respectively. Therefore, it can also be interpreted as a force balance equation. When the distribution of the random velocities is isotropic, the off-diagonal terms of $\boldsymbol{\Psi}$ become zero, but diagonal terms stays the same and equal to scalar pressure. Then, the equation (2.7) transforms to

$$mn\left[\frac{\partial \mathbf{u}}{\partial t}+(\mathbf{u}\cdot\nabla)\mathbf{u}\right]=-\nabla p+qn(\mathbf{E}+\mathbf{u}\times\mathbf{B})+\mathbf{S}_{ij} \tag{2.8}$$

where we have dropped out subscript $\mathbf{r}$ from equation (2.8)

The second-order moment : Equation of energy conservation, i.e., the second-order moment of the Boltzmann equation, is obtained by multiplying the equation (2.1) with $\frac{1}{2}mv^2$ and integrating over the velocity space:

$$\begin{aligned}\frac{m}{2}\int v^2\frac{\partial f}{\partial t}d\mathbf{v}+\frac{m}{2}\int v^2(\mathbf{v}\cdot\nabla_{\mathbf{r}})fd\mathbf{v}\\ +\frac{q}{2}\int v^2[(\mathbf{E}+\mathbf{v}\times\mathbf{B})\cdot\nabla_{\mathbf{v}}]fd\mathbf{v}=\int\frac{m}{2}v^2\left(\frac{\partial f}{\partial t}\right)_{coll.}d\mathbf{v}.\end{aligned} \tag{2.9}$$

Applying some mathematical procedures and using vector identities, the energy conservation equation can be written in several different forms. One of them is shown in the following [1]

$$\begin{aligned}\frac{\partial}{\partial t}\left[n\frac{1}{2}mu^2\right]+\nabla_{\mathbf{r}}\cdot\left[n\frac{1}{2}m<u^2\mathbf{u}>\right]-nq<\mathbf{E}\cdot\mathbf{u}>\\ =\frac{m}{2}\int u^2\left(\frac{\partial f}{\partial t}\right)_{coll.}d\mathbf{u}\end{aligned} \tag{2.10}$$

where the integral in the right hand side can also be labelled as $\mathbf{S_{coll.}}$. The terms in (2.10) represent the rate of change of energy density, the rate of energy loss per volume element due to heat transfer, the gained power from the electric field and collision term, respectively. It is noted that the collision term ($\mathbf{S_{coll.}}$) is not zero since the collisions between species lead to energy transfer among them. Moreover, there is no term including $\mathbf{B}$ because magnetic field does no work [30].

As stated before, the energy conservation equation can be written in several forms. Another one is

$$\frac{\partial}{\partial t}\left[n\frac{1}{2}m < w^2 >\right] + \nabla_{\mathbf{r}}\cdot\left[n\frac{1}{2}m < w^2 > \mathbf{u}\right] + (\mathbf{\Psi}\cdot\nabla_{\mathbf{r}})\cdot\mathbf{u} \\ +\nabla_{\mathbf{r}}\cdot\mathbf{q} = \mathbf{S_{coll.}} \tag{2.11}$$

where $\mathbf{w}$ is random (thermal) velocity, $\mathbf{q}$ is the heat flux or heat flow vector representing the heat flux resulting from random velocities of the particles. Furthermore, isotropic plasma can be considered to simplify the energy conservation equation. In this case, pressure tensor $\mathbf{\Psi}$ replaces with the scalar pressure p. When the first term representing average energy of the plasma is equal to $\frac{3}{2}k_BT$ and using $p = nk_BT$ where k_B is the Boltzmann constant, then the energy conservation equation reduces to a simpler form

$$\frac{\partial(\frac{3}{2}p)}{\partial t} + \nabla\cdot\left(\frac{3}{2}p\mathbf{u}\right) - p\nabla\cdot\mathbf{u} + \nabla\cdot\mathbf{q} = \mathbf{S_{coll.}} \tag{2.12}$$

where second term represents the divergence of flow of energy density at the fluid velocity in units of Wm^{-3} and third term is responsible for heat changes of the fluid because of compression or expansion of volume of fluid.

As a result, three moments of the Boltzmann equation can be written for each species of the plasma. These equations are also be supplied by Maxwell equations to complete a self-consistent fluid model.

2.1.2 Two-fluid equations with drift-diffusion approximation for fluxes

Complete set of two-fluid equations can be written by combining zeroth, first and second moments of the Boltzmann equation with Maxwell equations to have a self-consistent model. This model is called two-fluid because it interpretes electrons and ions separately and considers them as a continuum. When the isotropic case ($\nabla\cdot\mathbf{\Psi} = \nabla p$) and creation or vanishing of the charged particles are considered, the obtained equations are as in the following form:

$$\frac{\partial n_e}{\partial t} + \nabla\cdot(n_e\mathbf{u}_e) = S_e \tag{2.13}$$

$$m_en_e\left[\frac{\partial\mathbf{u}_e}{\partial t} + (\mathbf{u}_e\cdot\nabla)\mathbf{u}_e\right] = -\nabla p_e + q_en_e(\mathbf{E} + \mathbf{u}_e\times\mathbf{B}) + \mathbf{S}_{ei} + \mathbf{S}_{en} \tag{2.14}$$

$$\frac{\partial(\frac{3}{2}p_e)}{\partial t} + \nabla \cdot \left(\frac{3}{2}p_e\mathbf{u}_e\right) - p_e\nabla \cdot \mathbf{u}_e + \nabla \cdot \mathbf{q}_e = \mathbf{S_{coll.(e)}} \tag{2.15}$$

$$\frac{\partial n_i}{\partial t} + \nabla \cdot (n_i\mathbf{u}_i) = S_i \tag{2.16}$$

$$m_i n_i \left[\frac{\partial \mathbf{u}_i}{\partial t} + (\mathbf{u}_i \cdot \nabla)\mathbf{u}_i\right] = -\nabla p_i + q_i n_i(\mathbf{E} + \mathbf{u}_i \times \mathbf{B}) + \mathbf{S}_{ie} + \mathbf{S}_{in} \tag{2.17}$$

$$\frac{\partial(\frac{3}{2}p_i)}{\partial t} + \nabla \cdot \left(\frac{3}{2}p_i\mathbf{u}_i\right) - p_i\nabla \cdot \mathbf{u}_i + \nabla \cdot \mathbf{q}_i = \mathbf{S_{coll.(i)}} \tag{2.18}$$

Maxwell equations are

$$\nabla \times \mathbf{B} = \mu_0\mathbf{J} + \frac{1}{c^2}\frac{\partial \mathbf{E}}{\partial t} \tag{2.19}$$

$$\nabla \cdot \mathbf{B} = 0 \tag{2.20}$$

$$\nabla \times \mathbf{E} = -\frac{\partial \mathbf{B}}{\partial t} \tag{2.21}$$

$$\nabla \cdot \mathbf{E} = \frac{\sigma}{\epsilon_0} \tag{2.22}$$

Here n_e and n_i represent electron and ion densities, S_e and S_i are source terms and include the information of creation or vanishing of charged particles, $\mathbf{S_{coll.(e)}}$, $\mathbf{S_{coll.(i)}}$ are corresponding energy source terms due to collisions, ϵ_0 is the permittivity of free space, c is the speed of light, m_e, m_i are masses of the electrons and ions, p_e, p_i are pressures of the particles. σ and $\mathbf{J}$ represent the charge and the current density, respectively. The expressions for charge and current density can be written as

$$\sigma = n_i q_i + n_e q_e \tag{2.23}$$

$$\mathbf{J} = n_i q_i \mathbf{u}_i + n_e q_e \mathbf{u}_e \tag{2.24}$$

where q_e and q_i are charges of the electrons and ions, respectively. Meanwhile, the rate of change of momentum density due to collision between electrons and ions are written as

$$\mathbf{S}_{ei} = -m_e n_e \nu_{ei}(\mathbf{u}_e - \mathbf{u}_i) \tag{2.25}$$

where ν_{ei} is collision frequency between electron and ion particles [1]. $\mathbf{S}_{en}$, $\mathbf{S}_{ie}$, $\mathbf{S}_{in}$ can be constructed in a similar manner.

By using the definition of $\rho(\mathbf{r}, t) = mn(\mathbf{r}, t)$ where ρ is the mass density and m is the mass of a single particle for each species, the momentum equations (2.14) and (2.17) become as follows

$$\begin{aligned}\rho_e \frac{\partial \mathbf{u}_e}{\partial t} + \rho_e(\mathbf{u}_e \cdot \nabla)\mathbf{u}_e &= -\nabla p_e + en_e(\mathbf{E} + \mathbf{u}_e \times \mathbf{B}) \\ &-m_e n_e \nu_{en}(\mathbf{u}_e - \mathbf{u}_n) - m_e n_e \nu_{ei}(\mathbf{u}_e - \mathbf{u}_i)\end{aligned} \tag{2.26}$$

$$\begin{aligned}\rho_i \frac{\partial \mathbf{u}_i}{\partial t} + \rho_i(\mathbf{u}_i \cdot \nabla)\mathbf{u}_i &= -\nabla p_i + en_i(\mathbf{E} + \mathbf{u}_i \times \mathbf{B}) \\ &-m_i n_i \nu_{ie}(\mathbf{u}_i - \mathbf{u}_e) - m_e n_e \nu_{in}(\mathbf{u}_i - \mathbf{u}_n)\end{aligned} \tag{2.27}$$

where $\mathbf{u}_n$ is the average velocity of the neutral gas atoms.
In view of the fact that $m_e << m_i$, then it follows that $\rho_e(\mathbf{u}_e \cdot \nabla)\mathbf{u}_e << \rho_i(\mathbf{u}_i \cdot \nabla)\mathbf{u}_i$. In this case, the equation (2.26) can be simplified as follows

$$-\nabla p_e + en_e(\mathbf{E} + \mathbf{u}_e \times \mathbf{B}) - m_e n_e \nu_{en}(\mathbf{u}_e - \mathbf{u}_n) - m_e n_e \nu_{ei}(\mathbf{u}_e - \mathbf{u}_i) = 0. \tag{2.28}$$

For $\mathbf{u}_e >> \mathbf{u}_n, \mathbf{u}_i$ and $p_e = n_e k_B T_e$, above equation can be further reduced to

$$k_B T_e \nabla n_e + en_e \mathbf{E} + en_e(\mathbf{u}_e \times \mathbf{B}) + (m_e \nu_e) n_e \mathbf{u}_e = 0. \tag{2.29}$$

It can also be written in the form

$$n_e \mathbf{u}_e = -D_e \nabla n_e - \mu_e n_e \mathbf{E} - \mu_e n_e(\mathbf{u}_e \times \mathbf{B}) \tag{2.30}$$

where $\mu_e = e/m_e \nu_e$ is the electron mobility, $D_e = k_B T_e \mu_e / e$ is the electron diffusion coefficient [31], [32]. Here ν_e is the averaged electron collision frequency. It is taken approximately as $\nu_e = \nu_{en} + \nu_{ei}$.

Similarly, the momentum conservation equation for ionic species (2.17) can be written in the following form

$$-\nabla p_i + en_i(\mathbf{E} + \mathbf{u}_i \times \mathbf{B}) - m_i n_i \nu_{ie}(\mathbf{u}_i - \mathbf{u}_e) - m_i n_i \nu_{in}(\mathbf{u}_i - \mathbf{u}_n) = 0. \tag{2.31}$$

Assume that

$$\nu_{ie} m_i n_i(\mathbf{u}_i - \mathbf{u}_e) = -\nu_{ei} m_e n_e(\mathbf{u}_e - \mathbf{u}_i),$$

$$\mathbf{u}_n = 0,$$

and $m_e\nu_e << m_i\nu_{in}$. Then, equation (2.31) can be further reduced to

$$n_i\mathbf{u}_i = -D_i\nabla n_i + \mu_i n_i\mathbf{E} + \mu_i n_i(\mathbf{u}_i \times \mathbf{B}) \tag{2.32}$$

where $\mu_i = e/m_i\nu_i$ is the ion mobility and $D_i = k_B T_i\mu_i/e$ is the ion diffusion coefficient [31], [32].

When $\mathbf{B}$ is neglected and the above expressions for $n_e\mathbf{u}_e$ and $n_i\mathbf{u}_i$ in (2.30) and (2.32) are put into the contiunity equations (2.13) and (2.16), then the two-fluid equations with drift-diffusion approximation become

$$\frac{\partial n_e}{\partial t} + \nabla\cdot(-\mu_e n_e\mathbf{E} - D_e\nabla n_e) = S_e \tag{2.33}$$

$$\frac{\partial n_i}{\partial t} + \nabla\cdot(\mu_i n_i\mathbf{E} - D_i\nabla n_i) = S_i. \tag{2.34}$$

To have a self-consistent model, Eq. (2.33) and Eq. (2.34) are supplied with Poisson equation for electric potential

$$-\nabla^2\varPhi = \frac{e}{\epsilon_0}(n_i - n_e) \tag{2.35}$$

where $\varPhi$ is the potential of an electric field strength.

2.2 Simple and Extended Fluid Models

In this section, "simple" and "extended" fluid models are described. As previously mentioned, fluid models of glow discharges involve the continuity equation, momentum equation and energy equation for each plasma species. The system is also supplied with Poisson equation for the self-consistent electric field. In general, momentum equations of the fluid models are reduced to the drift-diffusion equations as it is done in Section 2.1.2. These equations include transport and rate coefficients, which represent the dynamics of the particles such as collisions between the particles. These coefficients are input data for the fluid models [33]. Since the reliability of any model is determined by its least accurately known element, determination of electrons' transport parameters and electron collision rates have a vital role in fluid models. In particular, the local-field approximation (LFA) and local-mean-energy approximation (LMEA) are usually utilized to incorporate transport and collision properties of the electrons into fluid models of gas discharge plasmas [12].

The equations for the gas discharge fluid model are

$$\frac{\partial n_k}{\partial t} + \nabla \cdot \mathbf{\Gamma}_k = S_k \tag{2.36}$$

$$\mathbf{\Gamma}_k = sgn(q_k)\mu_k n_k \mathbf{E} - D_k \nabla n_k \tag{2.37}$$

$$\epsilon_0 \nabla \cdot \mathbf{E} = \sum_k q_k n_k, \qquad \mathbf{E} = -\nabla \Phi \tag{2.38}$$

where k indicates the kth species such as electrons, ions, metastable atoms etc. $\mathbf{\Gamma}_k$ is the particle flux in drift-diffusion approximation.

These three equations form the model which we will call "simple fluid model" (see, e.g. [33]). In this model, transport coefficients (mobility and diffusion) and source terms (S_k) are defined as a function of the reduced electric field, $\mathbf{E}/p$ where $\mathbf{E}$ is the electric field magnitude and p is the background gas pressure. In the case of electron and ion species, source terms can be written in the form of $S_e = S_i = \alpha \mid \mathbf{\Gamma}_e \mid - \beta n_i n_e$; $\alpha = \alpha(E)$ is the coefficient of ionization by electron impact or the first Townsend coefficient, β is the coefficient of ion-electron recombination. This approach is called "local-field approximation" (LFA). In general, this approximation is not useful. The reason why this approach is unacceptable is that it does not take into account nonlocal ionization occuring in negative glow region and Faraday dark space. Since the ionization rate is a function of the local electric field strength in the LFA, it is expected that electron impact ionizations only occur in the cathode sheath, where the electric field strength is high enough. However, it is known that there exist ionizations in the regions of negative glow and Faraday dark space where the electric field strength is weak due to fast electrons from the cathode region. This phenomenon is called 'nonlocal ionization' and is not considered in the LFA. Therefore, the source of ions hitting the cathode for secondary electron emissions come not only from a high electric field regions but also from negative glow and Faraday dark space due to nonlocal ionizations. Note that the mobility and diffusion coefficients can be defined as constants but as functions of pressure by providing Einstein relation, $D/\mu = k_B T/e$ in simple fluid models.

In order to incorporate the effects of the nonlocal transport of electrons into the fluid models, "extended fluid model" approach [33] is developed by adding an electron energy equation to Eqs. (2.36), (2.37), (2.38), which is shown below

$$\frac{\partial n_\varepsilon}{\partial t} + \nabla \cdot \mathbf{\Gamma}_\varepsilon = -e\mathbf{\Gamma}_e \cdot \mathbf{E} - \frac{3}{2}\frac{m_e}{m_g}\nu_{ea} n_e k_B (T_e - T_g) - \sum_j \mathit{\Delta} E_j R_j \tag{2.39}$$

where $n_\varepsilon = n_e \frac{3}{2} k_B T_e$ is the electron energy density, $\mathbf{\Gamma}_\varepsilon$ is density of the electron energy flux and can be expressed as [33]

$$\mathbf{\Gamma}_\varepsilon = -D_\varepsilon \nabla n_\varepsilon - \mu_\varepsilon \mathbf{E} n_\varepsilon \tag{2.40}$$

where energy transport coefficients are related to transport coefficients via $D_\varepsilon = \frac{5}{3} D_e$ and $\mu_\varepsilon = \frac{5}{3}\mu_e$. In addition to these, the source terms in the right hand side of Eq. (2.39) are Joule heating (or cooling) of electrons in the electric field, the elastic loss and energy loss due to inelastic collisions, respectively. Meanwhile, ν_{ea} represents the electron-atomic elastic collision frequency, R_j is reaction rate corresponding to energy loss (or gain) $\mathit{\Delta} E_j$, m is the particle mass and T_g is the background gas temperature.

Extended fluid model is also known as "local-mean-energy approximation" [12] (LMEA). The transport and kinetic coefficients for electrons are defined as a function of electron temperature T_e by solving kinetic Boltzman equation. It is noted that the spatial distribution of electron temperature is obtained by the solution of electron energy equation. Since the source term of Eq. (2.39) is also responsible for the energy transfer by heat conduction, the nonlocality phenomenon of electrons can be handled more properly.

2.2.1 Basic plasma chemical reactions

In this work, three models are developed and analyzed. The first model, Model-1, is developed under the assumptions of "simple fluid model". The direct ionization and secondary electron emissions from cathode surface are only occuring reactions in "simple fluid model" and hence in Model-1. More detailed plasma-chemical model is employed in Model-2 and Model-3 by including different chemical reactions into the model. The Model-2 and Model-3 differentiate from one another in the set of reactions they include. Model-2 uses the first eighteen reactions in Table 2.1; however, Model-3 is an extended form of Model-2 by adding more excitation reactions (19), (20), (21), (22), (23), (24), (25) and (26).

Calculations are performed for a nitrogen gas. Seven species, namely, electrons, N_2^+ ions, excited nitrogen molecules; $N_2(a^{'}1)$, $N_2(A3, v0-4)$, $N_2(B3)$, $N_2(C3)$, and N_2 molecules are taken into account in Model-2 and Model-3, which are also summarized in Table 2.1. With respect to the processes between species, the reactions in Table 2.1 can be classified as elastic collision, direct ionization, excitation, relaxation. Elastic collisions are simplest collisions so that energy and momentum are conserved. Since the mass of electrons is much smaller than that of nitrogen molecules, the transfer of energy between them is negligible. Therefore, the only change is the direction of electron without significantly change in speed. The reaction (1) in Table 2.1 is an example of elastic collision. In contrast to elastic collision, all other electron collisions in Table 2.1 are inelastic [34]. The direct ionization is the most important reactions to sustain the glow discharge. For instance, in reaction (2), two produced electrons in the right hand side are accelerated by the electric field until another ionization is trigged. This multiplication of electrons occurs again and again and plays a vital role to maintain a glow discharge. The reactions (3)-(6) and (19)-(26) are examples of electron induced excitation reactions. Electron hits the nitrogen molecules with an energy transfer less than ionization energy, but enables the bounded electron to excite to a higher energy state. Since the excited molecules are unstable, the electron jumped a higher energy level tends to come back to its original ground state by radiating photon. This is called relaxation and the reactions (15)-(18) in Table 2.1 are examples of this phenomenon.

2.2.2 Transport coefficients

In Model-1, mobility and diffusion coefficients for electrons and ions are approximated by constants providing that they are related with Einstein relation, $D/\mu = k_B T/e$. In extended fluid models (Model-2, Model-3), mobility and diffusion coefficients for ions and excited molecules are also approximated by using the Einstein relation. However, the transport coefficients for electrons are calculated with the relations given in the reference [35] and shown below

$$\mu_e = -\frac{\gamma''}{3N}\int_0^\infty \frac{\varepsilon_k}{\widetilde{\sigma}_m}\frac{\partial F_0}{\partial \varepsilon_k}d\varepsilon_k \tag{2.41}$$

$$D_e = \frac{\gamma''}{3N}\int_0^\infty \frac{\varepsilon_k}{\widetilde{\sigma}_m}F_0 d\varepsilon_k \tag{2.42}$$

where $\widetilde{\sigma}_m$ is the effective momentum-cross-section taken from [36], ε_k is the electron kinetic energy in eV units, $\varepsilon_k = \frac{m_e v_e^2}{2e}$ and γ'' is $\sqrt{\frac{2e}{m_e}}$. F_0 is assumed to follow Maxwell distribution, $F_0(\varepsilon_k) = \frac{2}{\sqrt{\pi}}\frac{1}{T_e^{3/2}}exp(-\frac{\varepsilon_k}{T_e})$ and normalized with the help of $\int_0^\infty F_0(\varepsilon_k)\sqrt{\varepsilon_k}d\varepsilon_k = 1$. The electron-atomic elastic collision frequency is calculated by using the relation

$$\nu_{ea} = \frac{e}{m_e}\frac{1}{\mu_e} \tag{2.43}$$

Table2.1: List of chemical reactions used in Model-2 and Model-3

Index	Reaction	$\Delta E(eV)$	Rate coefficient	Reference
1	$e + N_2 \rightarrow e + N_2$	0	Cross section	[36]
2	$e + N_2 \rightarrow 2e + N_2^+$	15.6	Cross section	[36]
3	$e + N_2 \rightarrow e + N_2(a'1)$	8.4	Cross section	[36]
4	$e + N_2 \rightarrow e + N_2(A3, v0-4)$	6.17	Cross section	[36]
5	$e + N_2 \rightarrow e + N_2(B3)$	7.35	Cross section	[36]
6	$e + N_2 \rightarrow e + N_2(C3)$	11.03	Cross section	[36]
7	$e + N_2^+ \rightarrow 2N$	0	$2.8 \times 10^{-13}(T_g/T_e)^{0.5}m^3s^{-1}$	[37]
8	$e + N_2^+ \rightarrow N(^2\mathrm{D}) + N$	0	$3.7 \times 10^{-13}m^3s^{-1}$	[38]
9	$N_2(A3, v0-4) + N_2(A3, v0-4) \rightarrow N_2(B3) + N_2$	0	$7.7 \times 10^{-17}m^3s^{-1}$	[37]
10	$N_2(B3) + N_2 \rightarrow N_2(A3, v0-4) + N_2$	0	$5.0 \times 10^{-17}m^3s^{-1}$	[37]
11	$N_2(A3, v0-4) + N_2(A3, v0-4) \rightarrow N_2(C3) + N_2$	0	$3.0 \times 10^{-16}m^3s^{-1}$	[37]
12	$N_2(C3) + N_2 \rightarrow N_2(a'1) + N_2$	0	$1.0 \times 10^{-17}m^3s^{-1}$	[37]
13	$N_2(a'1) + N_2 \rightarrow N_2(B3) + N_2$	0	$2.0 \times 10^{-19}m^3s^{-1}$	[37]
14	$N_2(a'1) + N_2 \rightarrow 2N_2$	0	$2.0 \times 10^{-19}m^3s^{-1}$	[37]
15	$N_2(A3, v0-4) \rightarrow N_2 + h\nu(293nm)$	0	$5.0 \times 10^{-1}s^{-1}$	[39]
16	$N_2(B3) \rightarrow N_2(A3, v0-4) + h\nu(1045nm)$	0	$1.5 \times 10^{5}s^{-1}$	[39]
17	$N_2(C3) \rightarrow N_2(B3) + h\nu(336.5nm)$	0	$2.7 \times 10^{7}s^{-1}$	[39]
18	$N_2(a'1) \rightarrow N_2 + h\nu(177.1nm)$	0	$1.0 \times 10^{2}s^{-1}$	[39]
19	$e + N_2 \rightarrow e + N_2(A3, v5-9)$	7.0	Cross section	[36]
20	$e + N_2 \rightarrow e + N_2(A3, v10-)$	7.8	Cross section	[36]
21	$e + N_2 \rightarrow e + N_2(a''1)$	12.25	Cross section	[36]
22	$e + N_2 \rightarrow e + N_2(a1)$	8.55	Cross section	[36]
23	$e + N_2 \rightarrow e + N_2(B'3)$	8.16	Cross section	[36]
24	$e + N_2 \rightarrow e + N_2(E3)$	11.87	Cross section	[36]
25	$e + N_2 \rightarrow e + N_2(w1)$	8.89	Cross section	[36]
26	$e + N_2 \rightarrow e + N_2(W3)$	7.36	Cross section	[36]

2.2.3 Source terms

It is seen that there are source terms in the right hand side of Eq. (2.36) for each species of fluid model. These are taken as $S_e = S_i = \alpha \mid \mathbf{\Gamma}_e \mid$ for Model-1 since Model-1 considers only electrons and N_2^+ ions as plasma species. However, both of Model-2 and Model-3 include Eq. (2.36) for the electrons, N_2^+ ions, $N_2(a^{'}1)$, $N_2(A3, v0-4)$, $N_2(B3)$ and $N_2(C3)$. Because of this, source terms in the right hand side are determined by the reactions occuring in the discharge

$$S_k = \sum_i R_i - \sum_j R_j^{'} \tag{2.44}$$

where R_i is the creation rate and $R_j^{'}$ is the destruction rate of corresponding reactions.

Because of particle conservation, the source terms for electrons and ions are identical:

$$S_e = S_i = R_2 - R_7 - R_8 = K_2 n_e n_0 - K_7 n_e n_i - K_8 n_e n_i \tag{2.45}$$

Here, K_2, K_7 and K_8 represent the rate coefficients of the corresponding reactions (2), (7) and (8), respectively. Since the rates of reactions are proportional to the concentrations of the reacting particles, n_e, n_i, n_0, which are concentrations of electrons, ions and neutral atoms, appear in (2.45). It must be noted that indices of rates and rate coefficients correspond to the indices in the Table 2.1. The source terms for excited nitrogen molecules $N_2(a^{'}1)$, $N_2(A3, v0-4)$, $N_2(B3)$ and $N_2(C3)$ can be written as

$$\begin{aligned} S_m &= R_3 + R_{12} - R_{13} - R_{14} - R_{18} \\ &= K_3 n_e n_0 - K_{12} n_0 n_{m3} - K_{13} n_m n_0 - K_{14} n_m n_0 - K_{34} n_m \end{aligned} \tag{2.46}$$

$$\begin{aligned} S_{m1} &= R_4 + R_{10} + R_{16} - 2R_9 - 2R_{11} - 2R_{15} \\ &= K_4 n_e n_0 + K_{10} n_{m2} n_0 + K_{16} n_{m2} - 2K_9 n_{m1} n_{m1} - 2K_{11} n_{m1} n_{m1} \end{aligned} \tag{2.47}$$

$$\begin{aligned} S_{m2} &= R_5 + R_9 + R_{13} + R_{17} - R_{10} - R_{16} \\ &= K_5 n_e n_0 + K_9 n_{m1} n_{m1} + K_{13} n_m n_0 + K_{17} n_{m3} - K_{10} n_{m2} n_0 - K_{16} n_{m2} \end{aligned} \tag{2.48}$$

$$\begin{aligned} S_{m3} &= R_6 + R_{11} - R_{12} - R_{17} \\ &= K_6 n_e n_0 + K_{11} n_{m1} n_{m1} - K_{12} n_{m3} n_0 - K_{17} n_{m3} \end{aligned} \tag{2.49}$$

where subscripts m, m_1, m_2 and m_3 used with source and density terms correspond to $N_2(a^{'}1)$, $N_2(A3, v0-4)$, $N_2(B3)$ and $N_2(C3)$, respectively.

Reaction rate coefficients are given in Table 2.1. The coefficients from reactions (7) to (18) are approximated by constants or functions of T_e. However, the rate coefficients for the reactions from (1) to (6) and (19) to (26) are also calculated as a function of T_e by using the relation stated in the reference [35]

$$K_R = \gamma'' \int_0^\infty \varepsilon_k \sigma_R F_0 d\varepsilon_k \tag{2.50}$$

where K_R is the reaction rate coefficients for the reaction R. The corresponding cross sections σ_R for these reactions are taken from Boltzmann solver [36]. F_0 is electron energy distribution function (EEDF). It is assumed to follow Maxwell distribution.

As it is said before, Model-3 is constructed by adding some excitation reactions, from (19) to (26) in Table 2.1, into Model-2. The effects of these additional reactions show itself by the last source term in the right hand side of equation (2.39). $\varDelta E_j$ values are also given in the Table 2.1 and multiplication of these energy values with corresponding rates R_j take into account the effect of additional excitation reactions in Model-3. Thus, the difference between Model-2 and Model-3 comes from different $\sum_j \varDelta E_j R_j$ values in Eq. 2.39.

2.2.4 Boundary conditions

In Simple fluid model, Model-1, the boundary conditions for N_2^+ ions at the anode located at $x = 0$ and cathode located at $x = d$, where d is discharge length, are given below

$$n_i = 0 \tag{2.51}$$

i.e., ions are absent at the anode.

$$\widehat{\mathbf{n}} \cdot \mathbf{\Gamma}_i = 0 \tag{2.52}$$

i.e. no ion flow occurs at the cathode surface. The boundary conditions at the anode for electrons

$$\widehat{\mathbf{n}} \cdot \mathbf{\Gamma}_e = 0 \tag{2.53}$$

where electrons are absorbed. While at the cathode,

$$\mu_e n_e = \gamma \mu_i n_i \tag{2.54}$$

where γ is the rate of liberating electrons by hitting of ions on the cathode surface. It is called "secondary emission coefficient" as it is mentioned before.

In Extended fluid models, Model-2 and Model-3, the boundary conditions for N_2^+ ions and excited nitrogen molecules $N_2(a^{'}1)$, $N_2(A3, v0-4)$, $N_2(B3)$ and $N_2(C3)$ at the anode and cathode can be written as follows (see e.g. [40] and [41])

$$\widehat{\mathbf{n}} \cdot \mathbf{\Gamma}_i = \frac{1}{4} v_i n_i + a n_i \mu_i (\widehat{\mathbf{n}} \cdot \mathbf{E}) \tag{2.55}$$

$$\widehat{\mathbf{n}} \cdot \mathbf{\Gamma}_m = \frac{1}{4} v_m n_m \tag{2.56}$$

$$\widehat{\mathbf{n}} \cdot \mathbf{\Gamma}_{m1} = \frac{1}{4} v_{m1} n_{m1} \tag{2.57}$$

$$\widehat{\mathbf{n}} \cdot \mathbf{\Gamma}_{m2} = \frac{1}{4} v_{m2} n_{m2} \tag{2.58}$$

$$\widehat{\mathbf{n}} \cdot \mathbf{\Gamma}_{m3} = \frac{1}{4} v_{m3} n_{m3} \tag{2.59}$$

Here, the thermal velocity is defined as $v_j = \sqrt{8k_B T_j / \pi m_j}$ where j represent i, e, m $m1$, $m2$, $m3$. Particle flux $\mathbf{\Gamma}$ is defined by Eq. (2.35), $\widehat{\mathbf{n}}$ is a normal unit vector pointing towards the surface, a is a switching function and set to one if the direction of drift velocity is toward the wall; otherwise, it is set to zero:

$$a = \begin{cases} 1, & (\widehat{\mathbf{n}} \cdot \mathbf{E}) > 0 \\ 0, & (\widehat{\mathbf{n}} \cdot \mathbf{E}) \leq 0 \end{cases} \tag{2.60}$$

In the case of electrons, the boundary conditions at the anode and cathode are given as follows

$$\widehat{\mathbf{n}} \cdot \mathbf{\Gamma}_e = \frac{1}{4} v_e n_e \tag{2.61}$$

$$\widehat{\mathbf{n}} \cdot \mathbf{\Gamma}_e = \frac{1}{4} v_e n_e - \gamma \widehat{\mathbf{n}} \cdot \mathbf{\Gamma}_i \tag{2.62}$$

where γ is the secondary emission coefficient.

The boundary conditions at the anode and cathode for electron energy density are

$$\widehat{\mathbf{n}} \cdot \mathbf{\Gamma}_\varepsilon = \frac{1}{3} v_e n_\varepsilon \tag{2.63}$$

$$\widehat{\mathbf{n}} \cdot \mathbf{\Gamma}_\varepsilon = \frac{1}{3} v_e n_\varepsilon - 2 k_B T_e \gamma \widehat{\mathbf{n}} \cdot \mathbf{\Gamma}_i \tag{2.64}$$

It is noted that equations 2.61, 2.62 are consistent with equations 2.63, 2.64 since they are related to each other with the relation of $\widehat{\mathbf{n}} \cdot \mathbf{\Gamma}_\varepsilon = 2k_B T_e (\widehat{\mathbf{n}} \cdot \mathbf{\Gamma}_e)$ by the help of $D_\varepsilon = \frac{5}{3} D_e$ and $\mu_\varepsilon = \frac{5}{3} \mu_e$.

The boundary conditions of electric potential is the same for Model-1, Model-2 and Model-3. It is set $\varPhi = U_d$ at the anode and $\varPhi = 0$ at the cathode. U_d is an applied voltage. It is either defined explicitly or calculated by adding an external circuit to the model. Therefore, the model equations 2.36, 2.37, 2.38 and 2.39 are completed with an external circuit equation to obtain the voltage U_d at the anode.

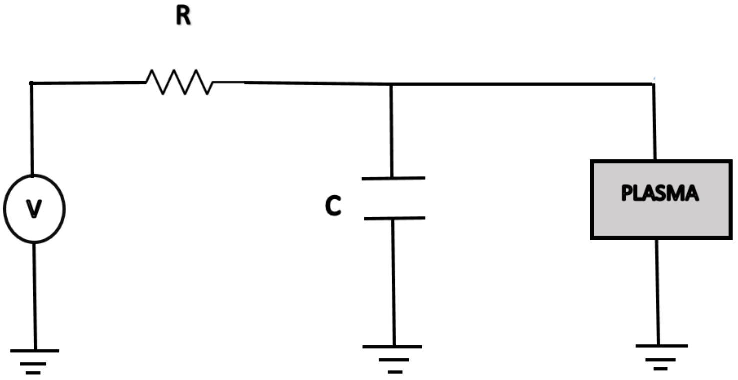

Figure 2.1: RC circuit used in Model-1, Model-2 and Model-3

The external circuit equation is

$$\frac{\mathrm{d}U_d}{\mathrm{d}t} + \frac{1}{C} \left(I_d - \frac{U_{src} - U_d}{R} \right) = 0 \tag{2.65}$$

where U_{src} is applied total voltage, R is the resistance of external circuit, I_d is discharge current and C is the external capacitance.

2.3 Comsol Multiphysics for modelling

The models are developed by using a commercial software, COMSOL Multiphysics version 5.2 [22]. "Transport of Diluted Species" from "Chemical Species Transport" module of COMSOL is used to define the fluid equations of Model-1. However, "General Form PDE" and "ODE and DAE" interfaces of "Mathematics" module are respectively used to define Poisson equation and external circuit equations in Model-1, Model-2 and Model-3. The fluid equations and electron energy equation are described with "General form PDE" in Model-2, Model-3.

The time-dependent solver is an implicit differential-algebraic solver. In the considered models, the time step is governed by the BDF (backward differential formula) solver. It uses backward differential methods for the integration of given equations. In each step of the integration, the nonlinear system is linearized by the help of Newton iteration method, so the nonlinear system transforms to the linear system of equations. The system of linear equations is solved with MUMPS, which stands for multifrontial massively parallel sparse direct solver [42]. This direct solver uses LU factorization of the coefficient matrix to find the solutions. The errors for this direct solver are controlled by choosing suitable values for relative and absolute tolerances. Apart from these, numerical grid is nonuniform and consists of 800 cells for each of the models to avoid singularities and degeneracies in the geometry [43].

In conclusion, in this chapter, the moments of the Boltzmann equation are evaluated to derive two-fluid equations with drift-diffusion approximation for fluxes. Poisson equation is also combined with these equations to have a self-consistent model. After defining governing equations of the plasma fluid theory, the three models, developed with COMSOL multiphysics software, are introduced. The Model-1 is developed under the assumptions of simple fluid approach (LFA), and the ideas of extended fluid approach (LMEA) are considered in Model-2 and Model-3. Hence, Model-2 and Model-3 are more detailed than Model-1. Indeed, Model-3 is the most detailed one since it is extended from Model-2 by adding additional reactions. Therefore, it is expected that the Model-3 must reflect the physical reality better than the Model-2 and the Model-1 for the analysis in the following chapters.

CHAPTER 3

COMPARISON OF THE MODELS AND THEIR APPLICABILITY

In this chapter, parameter regime and transport coefficients for each model are firstly introduced. It must be taken into consideration that all the calculations are made for DC supplied glow discharge plasma in nitrogen gas at 3 $Torr$ pressure. The verification of the three considered models (Model-1, Model-2 and Model-3) are made by comparing CVC curves for each model with experimental and computed data available from the literature. Finally, spatial distributions of plasma parameters corresponding to the three different DC regimes: abnormal, normal and subnormal are investigated to observe whether the models exhibit typical plasma behaviour under these regimes or not.

3.1 Parameter regime and transport coefficients

In this section, the parameters used in the numerical calculations are listed in the tables. Table 3.1 shows the parameters corresponding to Model-1, and Table 3.2 depicts the parameters corresponding to Model-2 and Model-3. It must be noted that the Townsend coefficient in Model-1 is a function of E/p since Model-1 uses the LFA approach. The relation for this coefficient is given as

$$\alpha = \alpha_0 exp(-E_0/ \mid E \mid) = Ape^{-Bp/|E|} \tag{3.1}$$

where $\alpha_0 = Ap$, $E_0 = Bp$ are constants and taken from the reference [6].

Table3.1: Parameters used in Model-1

Symbol	Value	Unit	Definition
d	0.01	m	discharge gap
p	3	$Torr$	pressure
μ_e	6.6672	$m^2/(Vs)$	electron mobility
μ_i	0.0233	$m^2/(Vs)$	ion mobility
D_e	6.6614	m^2/s	electron diffusion coefficient
D_i	5.828×10^{-4}	m^2/s	ion diffusion coefficient
α	$\alpha(E/p)$	m^{-1}	Townsend coefficient
α_0	3596.8	m^{-1}	Townsend coefficient constant
E_0	1.029×10^5	V/m	Townsend coefficient constant
γ	0.05	$-$	secondary emission coefficient
N_0	3.295×10^{22}	$1/(m^3Torr)$	gas density at 1 $Torr$
$T_g = T_i$	0.02499	eV	ion or gas temperature
T_e	1	eV	electron temperature

Table3.2: Parameters used in Model-2 and Model-3

Symbol	Value	Unit	Definition
d	0.01	m	discharge gap
p	3	$Torr$	pressure
μ_e	$\mu_e(T_e)$	$m^2/(Vs)$	electron mobility
μ_i	0.0520	$m^2/(Vs)$	ion mobility
D_e	$D_e(T_e)$	m^2/s	electron diffusion coefficient
D_i	0.00130	m^2/s	ion diffusion coefficient
D_m	0.00357	m^2/s	$N_2(a^{'}1)$ diffusion coefficient
D_{m1}	0.00357	m^2/s	$N_2(A3, v0-4)$ diffusion coefficient
D_{m2}	0.00357	m^2/s	$N_2(B3)$ diffusion coefficient
D_{m3}	0.00357	m^2/s	$N_2(C3)$ diffusion coefficient
ν_{ea}	$\nu_{ea}(T_e)$	$1/s$	elastic collision frequency
γ	0.05	$-$	secondary emission coefficient
N_0	3.295×10^{22}	$1/(m^3Torr)$	gas density at 1 $Torr$
$T_g = T_i$	0.02499	eV	ion or gas temperature

Unlike Model-1 where mobility and diffusion coefficients are approximated by constants, Model-2 and Model-3 define μ_e and D_e as functions of electron temperature T_e. The reason is that transport coefficients are developed by using the LMEA approach. Morever, the gas density value is given at pressure 1 $Torr$ in both tables. It can be scaled for any pressure using the relation $N_g = pN_0$ where N_g is gas density at the interested pressure.

3.2 Current-voltage characteristics of the models

Current-voltage characteristics (CVC) obtained from the considered models are analyzed by comparing them with the experimental and computed CVC curves. Three CVC curves from Model-1, Model-2 and Model-3 and four reference plots from literature are collected in the same graph in Figure 3.1.

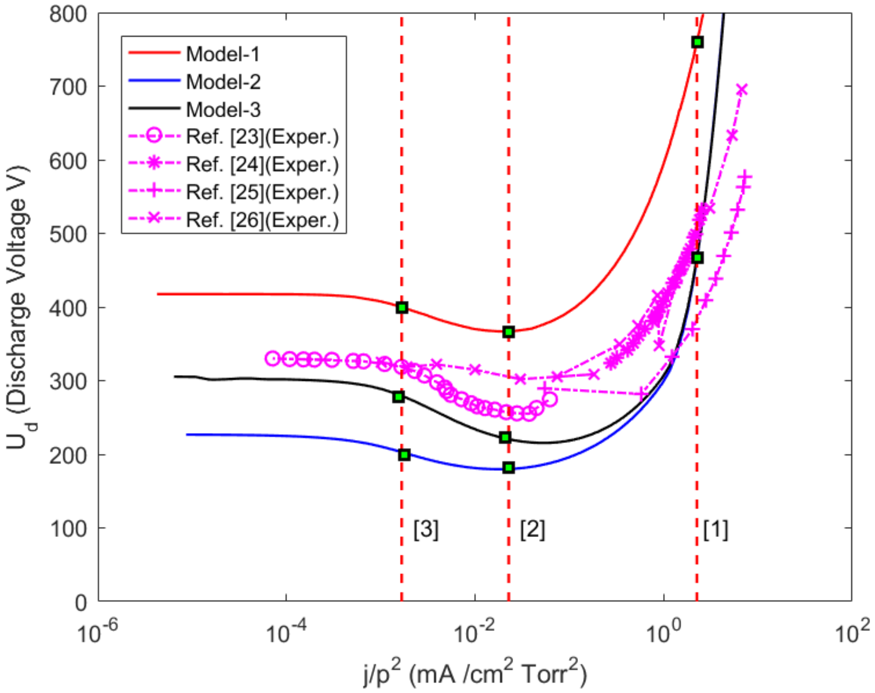

Figure 3.1: CVC curves obtained from the Model-1, Model-2, Model-3 and from the Experiment [23], [24], [25], and [26]

The horizontal axis represents the reduced current density j/p^2, and the vertical axis represents the anode voltage U_d. Current density and anode voltage, forming CVC curves, are calculated by changing the resistance of the external circuit and holding capacitance and applied voltage constant. Actually, this is the reason why the external circuit is added to the developed models. Otherwise, all the solutions converge to the abnormal regime so that the calculations for normal and subnormal regime cannot be carried out. In Figure 3.1, it is shown that the CVC curves obtained from the Model-1, Model-2 and Model-3 are qualitatively in agreement with the curves obtained from the references. This means that developed three models with corresponding parametric regimes stated in Section 3.1 are applicable to explore the basic properties of DC supplied nitrogen discharge plasma. The CVC curve for Model-3 demonstrates the best result since it is the closest one to the experimental data from the literature [23], [24], [25], and [26]. Indeed, the CVC curve for Model-2 is also applicable, and curve for Model-1 reflects the characteristic behaviour of the system.

As it is shown in Figure 3.1, three vertical lines are drawn and labelled with numbers 1, 2 and 3. The intersection points between these lines and CVC curves indicate three typical glow discharge regimes. These are abnormal, subnormal and normal regimes, respectively. The current density (j) and discharge voltage (or anode voltage) (U_d) corresponding to these intersection points are shown in Table 3.3. The spatial distributions of discharge characteristics corresponding to the three regimes indicated in Table 3.3 are analyzed in the following section.

Table3.3: $j(mA/cm^2)$, $U_d(V)$ values corresponding to the three regimes: subnormal, normal and abnormal

Models	Parameters	Subnormal	Normal	Abnormal
Model-1	$j(mA/cm^2)$	0.0148	0.2043	20.45
	$U_d(V)$	399.68	366.78	765.82
Model-2	$j(mA/cm^2)$	0.0148	0.2043	20.45
	$U_d(V)$	203.22	179.93	467.54
Model-3	$j(mA/cm^2)$	0.0148	0.2043	20.45
	$U_d(V)$	279.64	220.45	470.14

3.3 Spatial distributions of basic plasma parameters

Spatial distributions of plasma parameters computed from Model-1, Model-2 and Model-3 are investigated at the three typical regimes. As it is mentioned before, the intersection points between the vertical lines 1, 2, 3 and CVC curves obtained from three considered models indicate the abnormal, normal and subnormal regimes, respectively.

Abnormal regime: The calculations are done at the regime corresponding to the intersection points between the vertical line 1 and CVC curves derived from the models. The corresponding reduced current density and current density are 2.272 $mA/(cm^2 Torr^2)$ and 20.45 mA/cm^2, respectively.

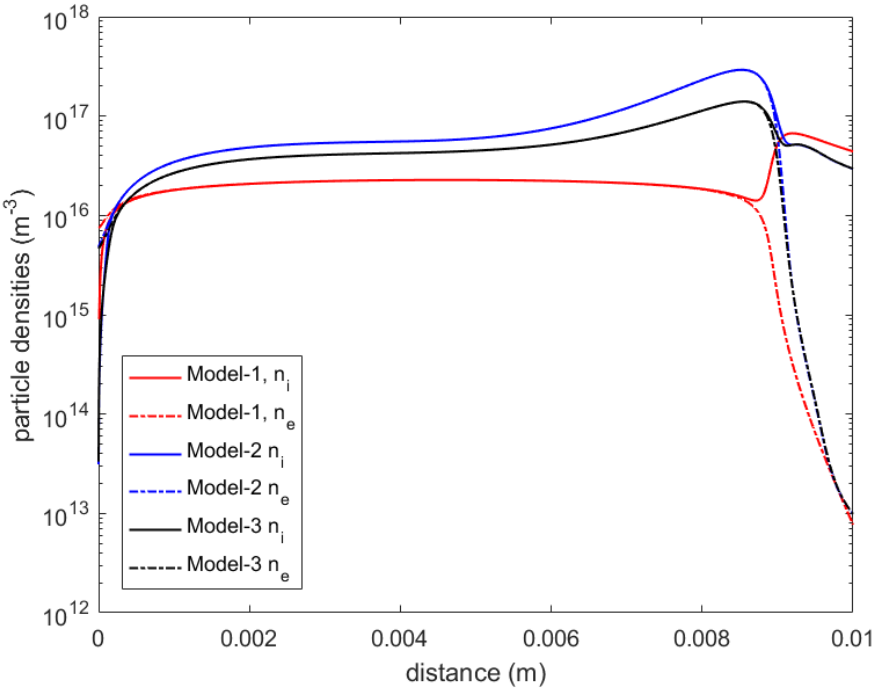

Figure 3.2: Spatial distributions of particle densities n_e, n_i corresponding to the three models. Parameters are given in Tables 3.1, 3.2

Fig. 3.2 represents the spatial distributions of particle densities n_e, n_i for each model. It is seen that cathode layer width of abnormal regime is smaller than that of other regimes (see cathode layer in Fig. 3.8 and Fig. 3.14). Moreover, most part of the space in the tube is quasineutral, $n_e \approx n_i$. It is seen that ionization of N_2 molecules mainly occurs in the narrow cathode sheath region since the electric field has large values at this region (see Figure 3.5). Therefore, the ionization rates have peaks at the right part of the Fig. 3.3.

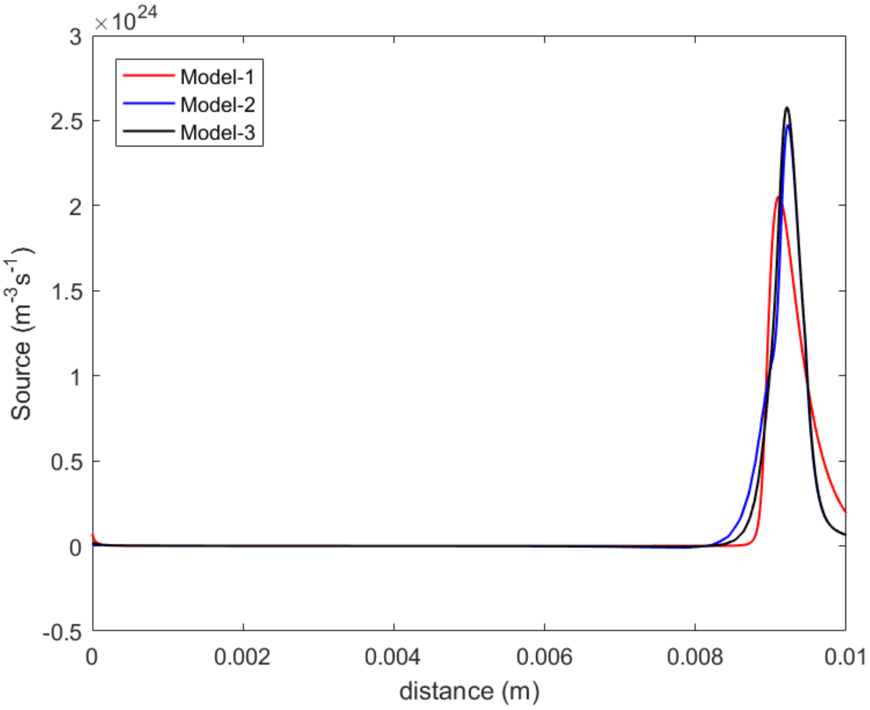

Figure 3.3: Spatial distributions of ionization rates corresponding to the three models. Parameters are the same as in Figure 3.2

The spatial distributions of electric potential Φ are illustrated in Figure 3.4. The voltage value hardly ever decreases in quasineutral region due to small charge density. However, there is a dramatic voltage drop at the vicinity of cathode since ion density is higher than electron density at this region. The reason why the ion density is higher than the electron density near the cathode is that the mobility of electrons is higher than that of ions, so they move more rapidly towards the electrodes in the presence of electric field and leave the region positively charged. When the electric field profile, shown in Figure 3.5, is examined, the strength of the electric field in the plasma region is small, but it rapidly increases to the order of 10^5 V/m at the cathode sheath.

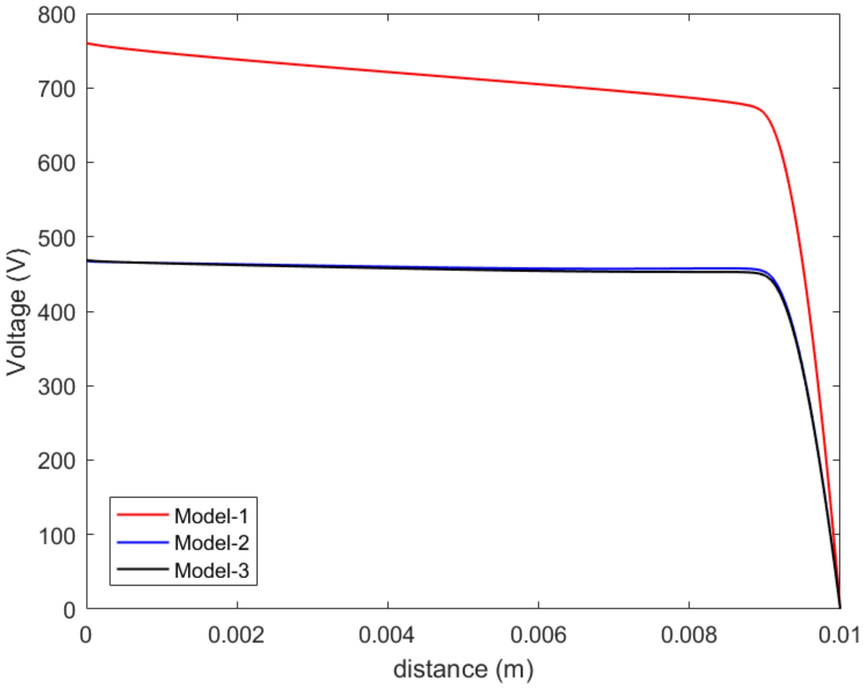

Figure 3.4: Spatial distributions of electric potential Φ corresponding to the three models. Parameters are the same as in Figure 3.2

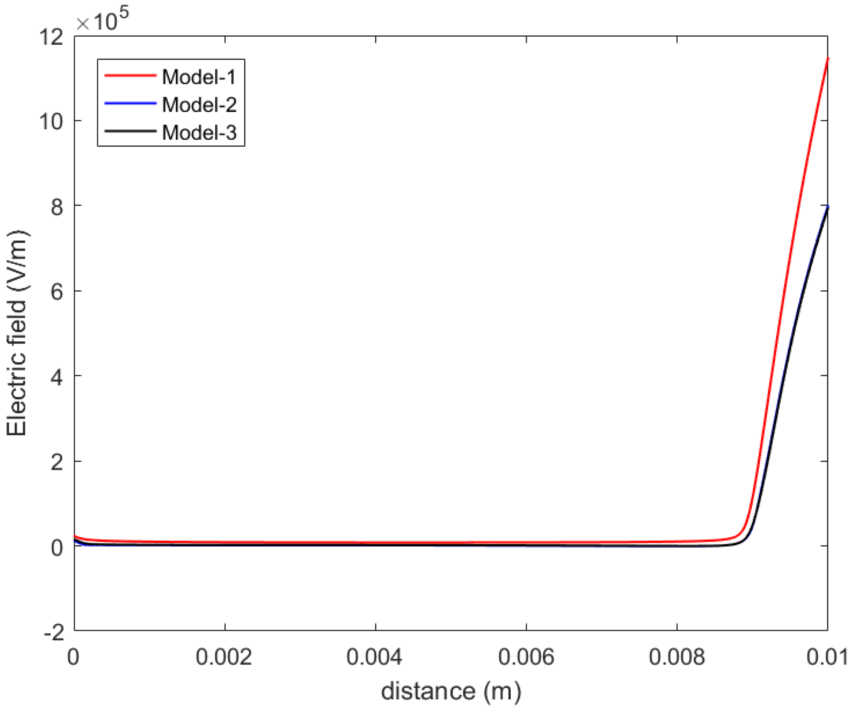

Figure 3.5: Spatial distributions of electric field E corresponding to the three models. Parameters are the same as in Figure 3.2

In Fig. 3.6, the spatial distributions of electron, ion and total current densities j_e, j_i and j_t in abnormal regime are depicted. Since the ions coming from anode region are accelerated by the high electric field near the cathode, the ion current density increases at this region. Unlike ion current density, decreasing of absolute electron current density does not mean the electron current density decreases near the cathode. This says that electrons are accelerated in backward direction, from cathode to anode. It is noted that a constant total current density for each of the models represents the verification of charge conservation along the discharge tube.

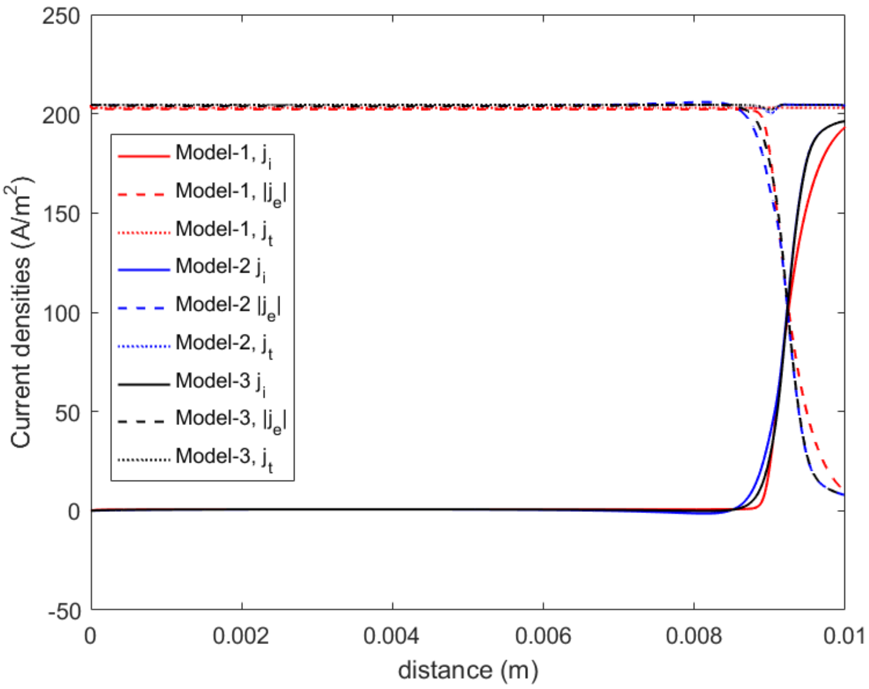

Figure 3.6: Spatial distributions of current densities $|j_e|$, j_i and j_t corresponding to the three models. Parameters are the same as in Figure 3.2

The spatial distributions of electron temperature T_e for Model-2 and Model-3 are illustrated in Figure 3.7. The electrons are induced from the cathode surface by hitting N_2^+ ions or generated in the ionizations. The produced electrons gain energy from the electric field in the cathode sheath region and the temperatures of them reach the values between 80 and 90 eV in abnormal regime. These fast electrons accounts for not only initiating the reactions for sustaining the discharge but also the current of the system.

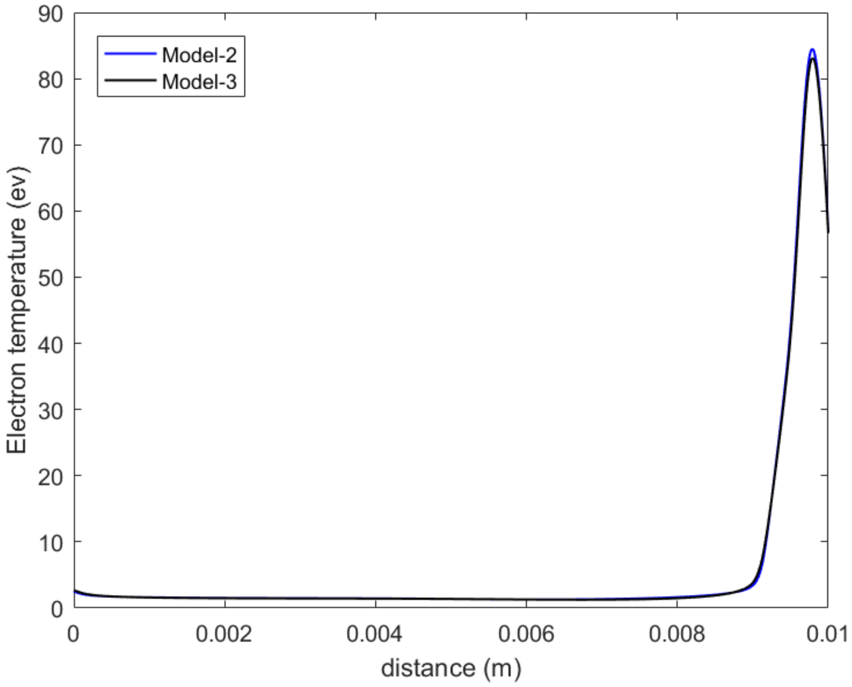

Figure 3.7: Spatial distributions of electron temperature T_e corresponding to the two models. Parameters are the same as in Figure 3.2

Normal regime: The calculations for normal regime are done for the regime corresponding to the intersection points between vertical line 2 and CVC curves derived from three models in Figure 3.1. In this regime, reduced current density is 0.0227 $mA/(cm^2 Torr^2)$, and current density is 0.2043 mA/cm^2.

Figure 3.8 represents the spatial distributions of particle densities n_e, n_i for each of the considered models in normal regime. It must be noted that cathode sheath region becomes wider and quasineutral region becomes narrower than corresponding regions observed for abnormal regime. The ionization of nitrogen molecules occurs in a wider space near the cathode as it is shown in Figure 3.9. Therefore, ionization rate curves become broader in cathode sheath region than abnormal ionization rate curves in Figure 3.3.

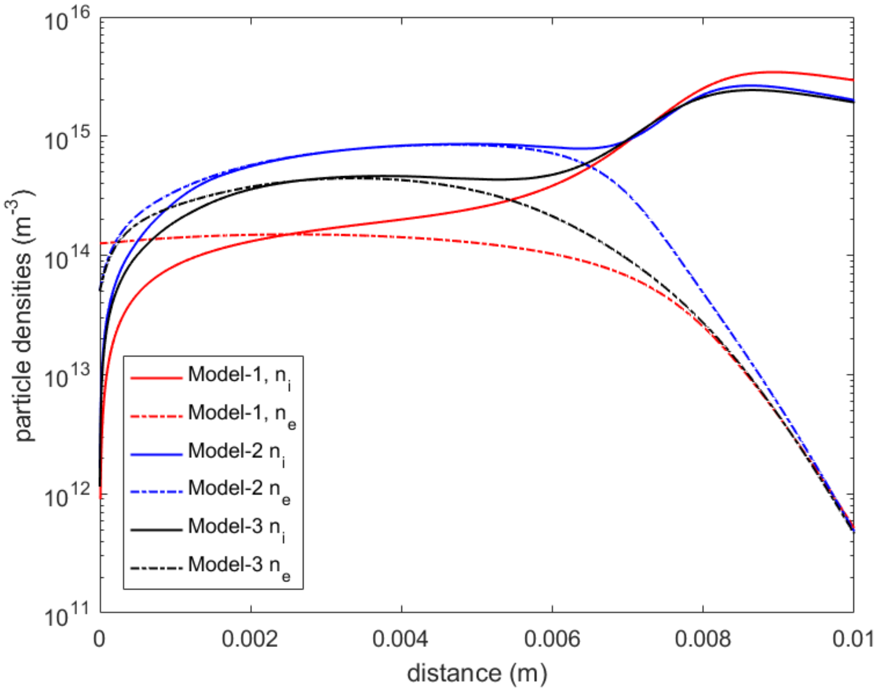

Figure 3.8: Spatial distributions of particle densities n_e, n_i corresponding to the three models. Parameters are listed in Tables 3.1, 3.2

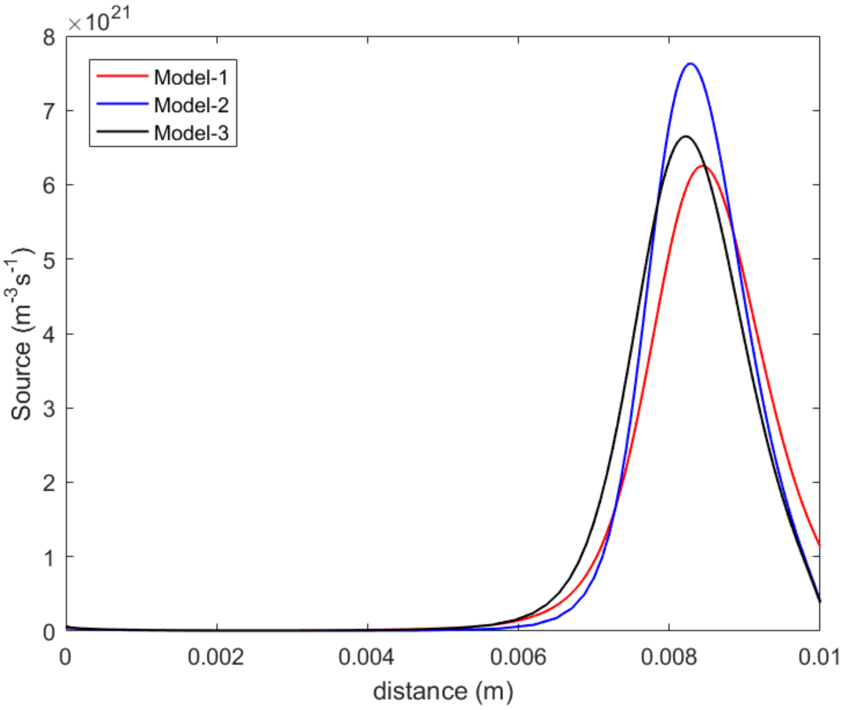

Figure 3.9: Spatial distributions of ionization rates corresponding to the three models. Parameters are the same as in Figure 3.8

The spatial distributions of electric potential Φ are illustrated in Figure 3.10. As it is expected that voltage drop is not dramatic in quasineutral region, and voltage drop in cathode sheath is smoother compared with that in Figure 3.4. Moreover, the anode voltage (located at $x = 0$ for each model) for this regime takes the smallest value compared to anode voltage from other two regimes because the intersection point for the normal regime in Figure 3.1 corresponds to nearly local minimum of CVC curves. In Figure 3.11, electric field E profiles are shown. The strength of the electric field increases in the cathode sheath region but cannot reach as high values as in abnormal regime. This explains why we have smaller particle density, ionization rate values in normal regime when these are compared with the results from abnormal regime.

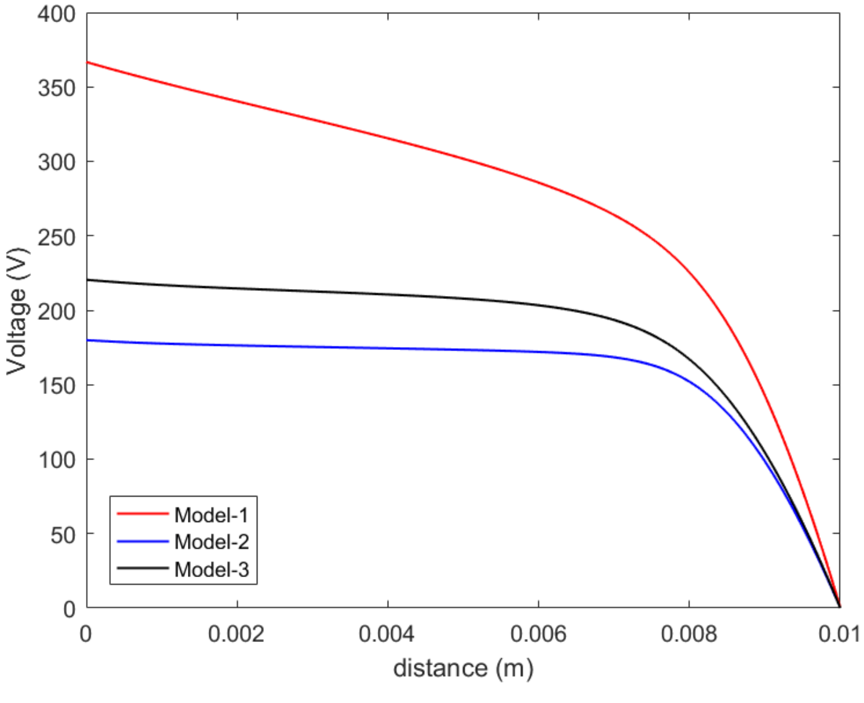

Figure 3.10: Spatial distributions of electric potential Φ corresponding to the three models. Parameters are the same as in Figure 3.8

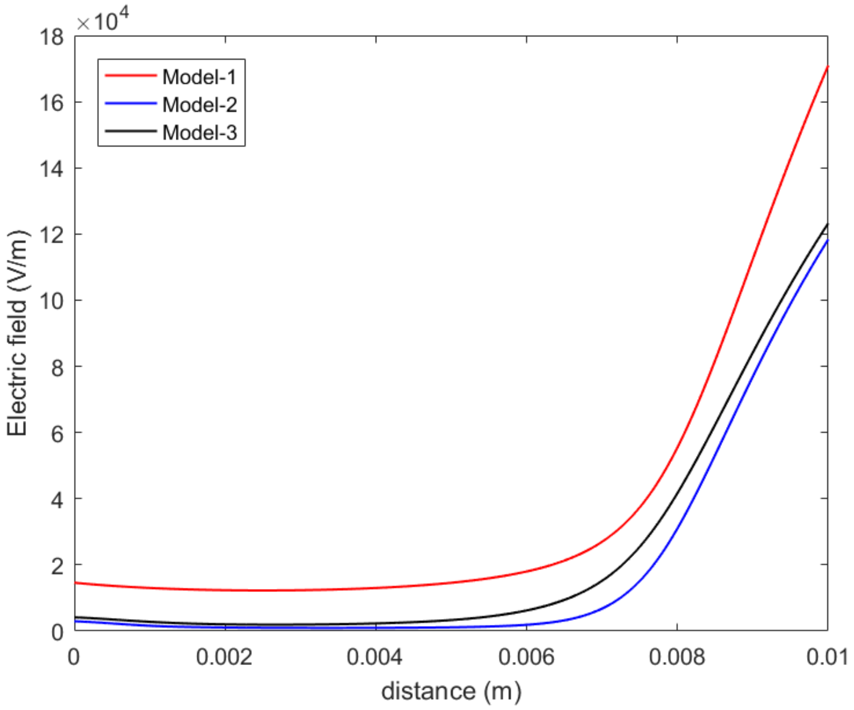

Figure 3.11: Spatial distributions of electric field E corresponding to the three models. Parameters are the same as in Figure 3.8

Spatial distributions of electron, ion and total current densities in normal regime are depicted in Figure 3.12. Since particles are less accelerated by electric field than in the abnormal regime, the current densities under the normal regime take smaller values than that in the abnormal regime in Figure 3.6. Verification of charge conservation can also be proved by a constant total current density in Figure 3.12. In addition, Figure 3.13 shows spatial distributions of electron temperature T_e obtained from Model-2 and Model-3. Since the strength of electric field is lower than abnormal regime, the temperature of electrons in normal regime are smaller than that in abnormal regime both for Model-2 and Model-3.

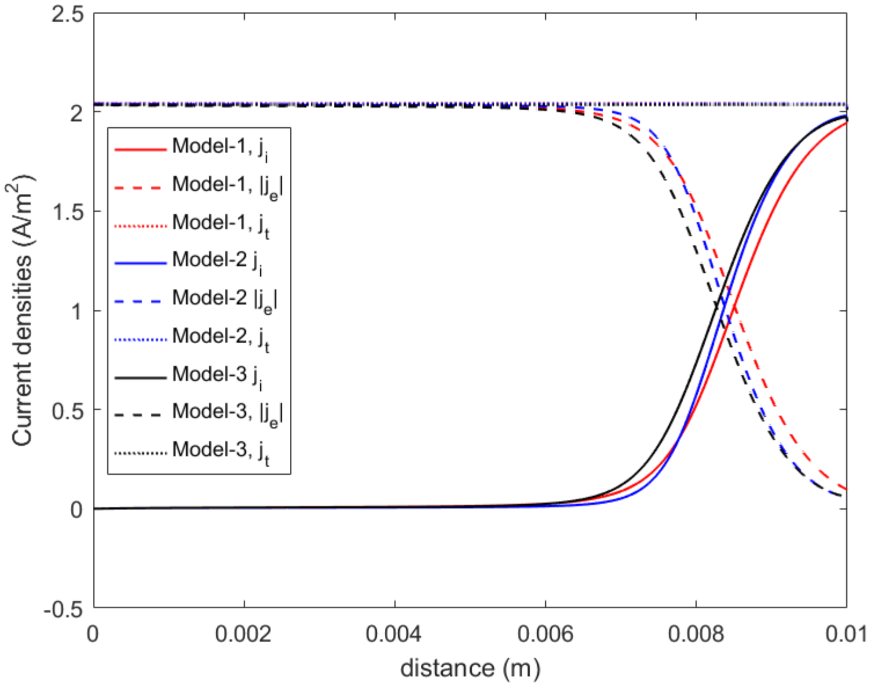

Figure 3.12: Spatial distributions of current densities $|j_e|$, j_i and j_t corresponding to the three models. Parameters are the same as in Figure 3.8

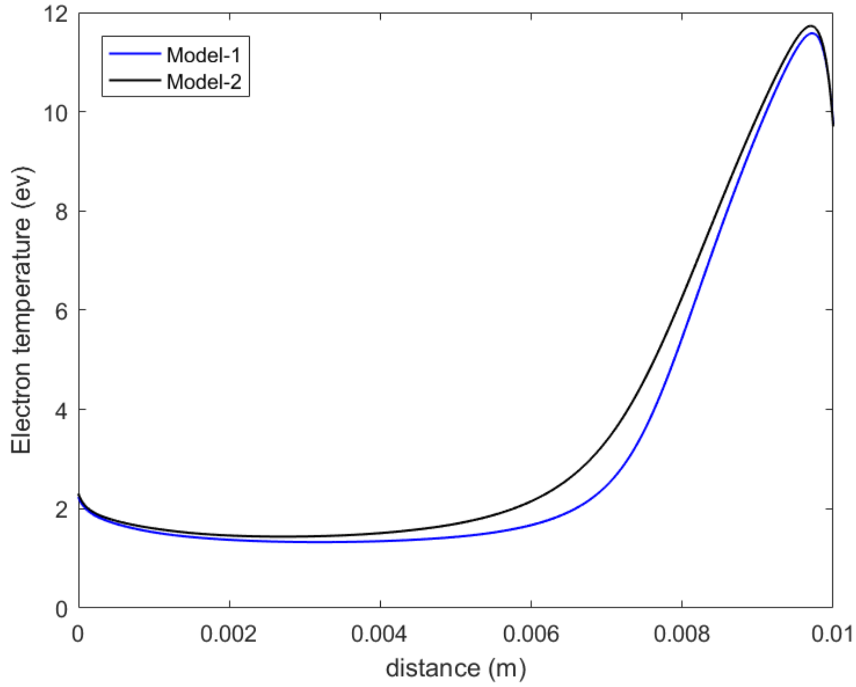

Figure 3.13: Spatial distributions of electron temperature T_e corresponding to the two models. Parameter are the same as in Figure 3.8

Subnormal regime: The calculations for subnormal regime are done at the conditions corresponding to intersection points between vertical line 3 and CVC curves in Figure 3.1. In this regime, the reduced current density and current density are 0.00164 $mA/(cm^2Torr^2)$ and 0.0148 mA/cm^2, respectively.

The spatial distributions of particle densities n_e, n_i for Model-1, Model-2 and Model-3 are illustrated in Figure 3.14. Quasineutral region hardly exists in this regime, and the ionization rate curves in Figure 3.15 are broaden along the discharge tube.

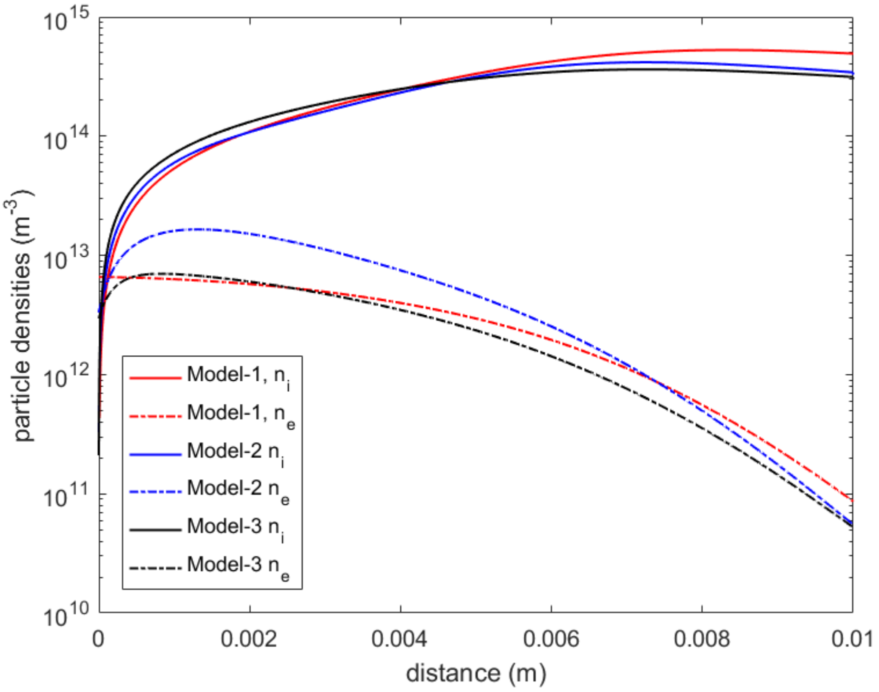

Figure 3.14: Spatial distributions of particle densities n_e, n_i corresponding to the three models. Parameters are listed in Tables 3.1, 3.2

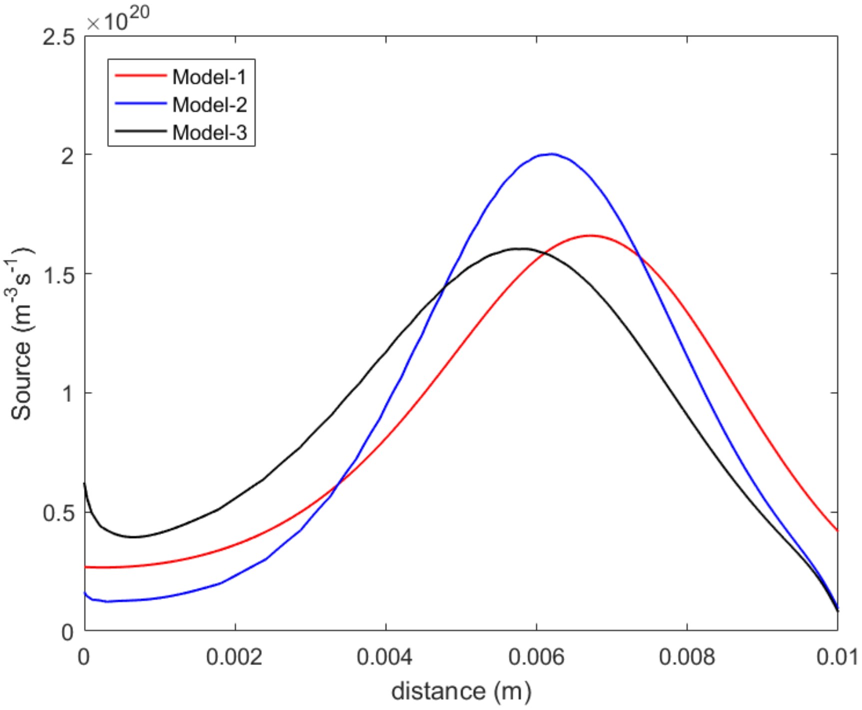

Figure 3.15: Spatial distributions of ionization rates corresponding to the three models. Parameters are the same as in Figure 3.14

Figure 3.16 shows the spatial distributions of the electrical potential Φ in the subnormal regime. Since quasineutral region does not exist in this regime, there is a smooth voltage drop along the tube. Corresponding electric field profile is depicted in Figure 3.17. In consistency with decreasing potential from anode to cathode, electric field strength smoothly increases across the tube. In detail, the magnitude of electric field is not zero along the tube.

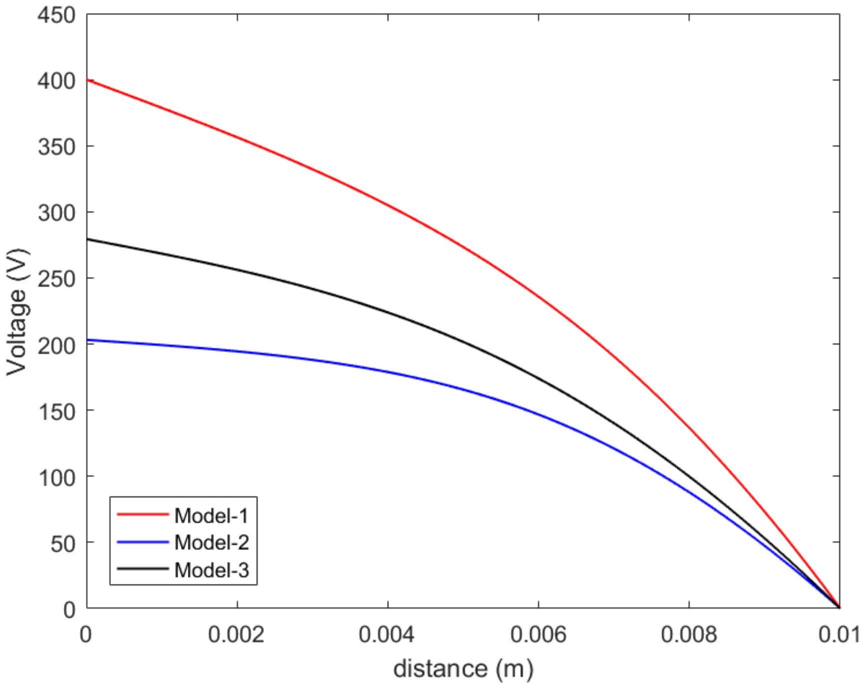

Figure 3.16: Spatial distributions of electric potential Φ corresponding to the three models. Parameters are the same as in Figure 3.14

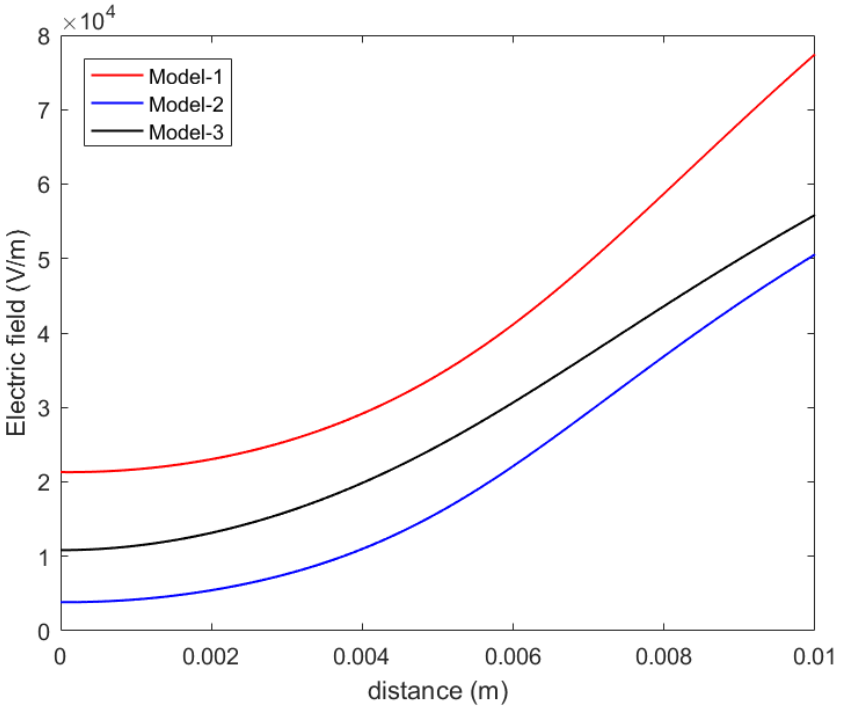

Figure 3.17: Spatial distributions of Electric field E corresponding to the three models. Parameters are the same as in 3.14

In Figure 3.18, the spatial distributions of electrons, ions and total current densities j_e, j_i and j_t obtained from three models are demonstrated. Charge conservation can be again observed from the uniformity of the total current j_t. Moreover, the values of current densities in subnormal regime take smaller values than those of current densities in abnormal and normal regimes because particles are less accelerated by electric field stated in Figure 3.17 than other two regimes.

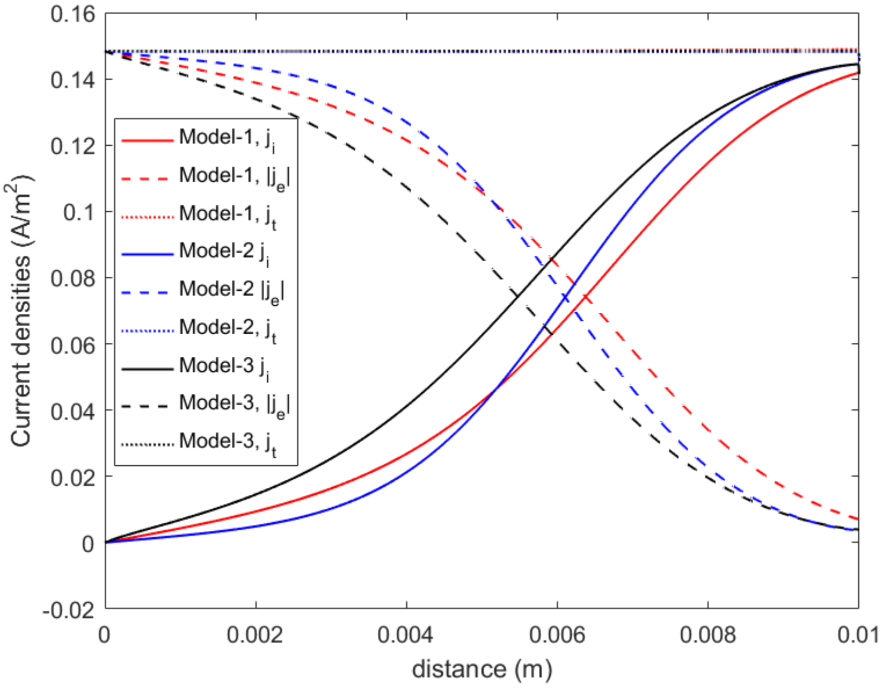

Figure 3.18: Spatial distributions of current densities $|j_e|$, j_i and j_t corresponding to the three models. Parameters are the same as in Figure 3.14

The spatial distributions of electron temperature for Model-2, Model-3 are given in Figure 3.19. The electron temperature under subnormal regime takes smaller values than in normal and abnormal regimes because of weaker electric field strength than at abnormal and normal regimes.

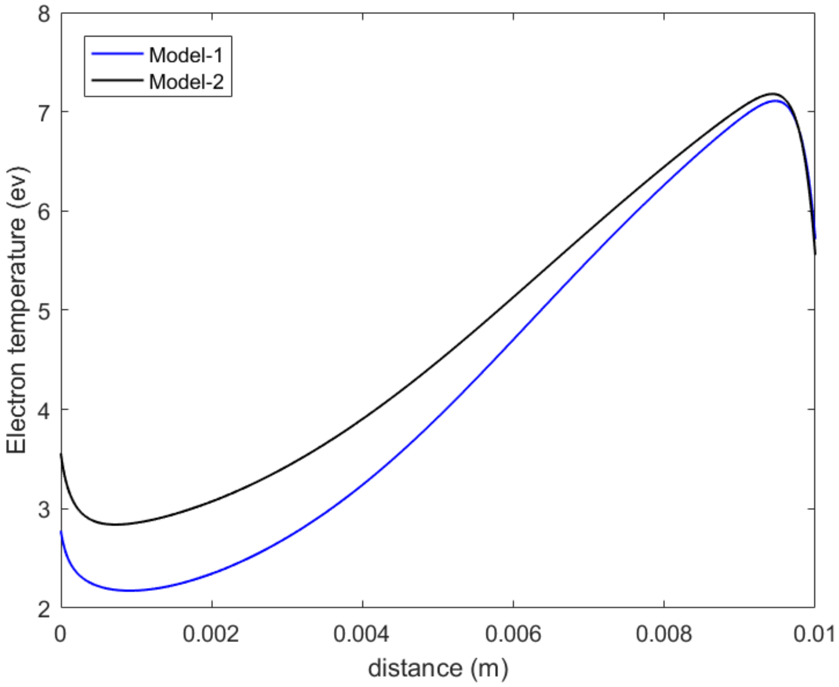

Figure 3.19: Spatial distributions of electron temperature T_e corresponding to the two models. Parameters are the same as in Figure 3.14

In conclusion, in this chapter, the models are developed to explore the basic properties of DC supplied nitrogen discharge plasma. It is seen that CVC curves obtained from the models are qualitatively in agreement with the experimental plots available from literature. The CVC curve from Model-3 is the most compatible one with the experimental curves from [23], [24], [25], and [26]. This result is expected because Model-3 includes more extensive set of reactions than Model-2, Model-1, so it is the most detailed one. Moreover, the spatial distributions of plasma parameters for each model are investigated at the three typical regimes: abnormal, normal and subnormal. The results show that the models exhibit expected typical plasma behaviour under these regimes. Finally, it is remarked that these models are applicable to explore the basic properties of DC supplied nitrogen discharge plasma.

CHAPTER 4

NUMERICAL MODELLING OF THE GAS DISCHARGE-SEMICONDUCTOR SYSTEM (GDSS) IN NITROGEN

A system consists of a planar gas discharge coupled with a semiconductor layer. Experiments exhibit a variety of spatiotemporal patterns in this system [21]. In this chapter, the spatial and the temporal changes in the transversal directions are assumed negligible so that the developed models are one dimensional. Hence, the only changes occur in the direction, perpendicular to the planar electrodes, with time. In Section 4.1, the parameter regime and input parameters are defined, the equation for semiconductor layer is introduced and the results in dimensionless form are discussed. Section 4.2 accounts for qualitative changes of the numerical results with respect to control parameter in an effort to determine whether the solutions are stable or unstable. In Section 4.3, the bifurcation curves for each model are developed and compared with experimental data. The type of bifurcations are also specified and discussed.

4.1 Parameter regimes and non-dimensional definitions

In Section 3.1, the parameter regimes for the considered models are represented in the tables: Table 3.1 for Model-1, Table 3.2 for both Model-2 and Model-3. In this chapter, the same plasma models are used for series of calculations. However, the parameters are consistent to the experiments described in the references [27], [20]. Pressure of the nitrogen gas is 40 *mbar*, discharge gap width is 1 *mm* and secondary emission coefficient is 0.08 for each of the considered models. These three parameters play a vital role for the behaviour of the discharges. Mobility and diffusion coefficients for ions, electrons and excited molecules are rescaled by multiplying the corresponding values given in Tables 3.1 and Table 3.2 with (p_0/p) where p is the pressure, 40 $mbar$ (or 30 $Torr$) and p_0 is 3 $Torr$ in this case. Corresponding elastic collision frequencies, ν_{ea}, for Model-2 and Model-3 are rescaled by multiplying with (p/p_0). Apart from these, α_0 and E_0 stated in Table 3.1 for Model-1 are modified by multiplying them with (p/p_0) since both of them are directly proportional to the pressure of the system and thereby affect the value of Townsend coefficient because of the relation given in equation 3.1

In addition to above parametric changes, the gas discharge is coupled to a semiconductor layer of GaAs, which plays a role of cathode. This system has been considered in many experimental and theoretical/ numerical studies [19], [21], and [20]. The schematic illustration is shown in Figure 4.1.

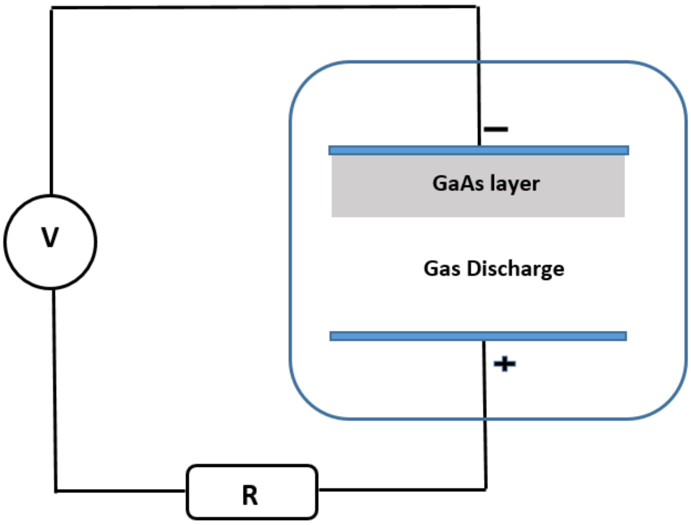

Figure 4.1: The schematic illustration of a planar gas discharge coupled with a semiconductor layer

It is assumed that the conductivity σ_s and the dielectricity constant ϵ_s for the semiconductor layer are constants. This means that the homogeneity of the total current is not affected along the semiconductor layer. The equation of charge conservation for one dimensional system in the x direction perpendicular to the electrode can be written as

$$\frac{\partial q_s(t)}{\partial t} + \frac{\partial J_s(t)}{\partial x} = 0 \tag{4.1}$$

where $q_s(t) = \epsilon_s \epsilon_0 \frac{\partial E_s(t)}{\partial x}$ follows from the Gauss law for the semiconductor layer with a dielectricity constant ϵ_s, and $J_s(t) = \sigma_s E_s(t)$ from the Ohm' s law for the semiconductor layer with a constant conductivity σ_s. Then,

$$\frac{\partial}{\partial x}\left(\epsilon_s \epsilon_0 \frac{\partial E_s(t)}{\partial t} + J_s(t)\right) = 0 \tag{4.2}$$

The relation inside the paranthesis must be constant with respect to x variable. This constant physically corresponds to the total current density $J(t)$. Therefore, the equation 4.2 becomes

$$\epsilon_s \epsilon_0 \frac{\partial E_s(t)}{\partial t} + J_s(t) = J(t) \tag{4.3}$$

and the voltage and electric field along semiconductor are related as it is shown below

$$U_s(t) = E_s(t) d_s. \tag{4.4}$$

With the help of $J_s(t) = \sigma_s E_s(t)$, the equation (4.3) and (4.4) can be written in terms of macroscopic parameters

$$C_s \frac{\partial U_s(t)}{\partial t} + J_s(t) = J(t) \tag{4.5}$$

$$U_s(t) = R_s(t) J_s(t) \tag{4.6}$$

respectively. The corresponding macroscopic relations are

$$C_s = \frac{\epsilon_s \epsilon_0}{d_s}, \quad R_s = \frac{d_s}{\sigma_s}$$

where C_s is the capacitance per area, R_s is the resistance of the semiconductor. Maxwell time scales can also be written in the form

$$T_s = C_s R_s = \frac{\epsilon_s \epsilon_0}{\sigma_s}$$

where T_s is the time that the charge needs to cross the semiconductor layer.

The total stationary voltage over the complete system is $U_t = U(t) + U_s(t)$ where $U(t)$ corresponds to the discharge voltage. By using this relation and multiplying both sides of the equation (4.5) with R_s, the equation (4.5) becomes

$$T_s \frac{\partial U(t)}{\partial t} - U_t + U(t) + R_s J(t) = 0 \tag{4.7}$$

It must be noted that Equation (4.7) is in the same form as the external circuit equation given in Chapter 2. This means that the specific structure for the semiconductor layer is not necessary to be included into the model for one dimensional investigation of the oscillations. Instead of that, any serial external circuit connected to the discharge will support the same equation (4.7). In the calculations described in this chapter, the width of semiconductor layer is $d_s = 1.5\ mm$, the dielectricity constant $\epsilon_s = 13.1$. In Section 4.2, the conductivity is taken as $\sigma_s = 2.4 \times 10^{-7}\ (\Omega cm)^{-1} = 2.4 \times 10^{-5}\ (S/m)$ that corresponds to the resistance of semiconductor $R_s = 62.5\ \Omega m^2$. Experimentally, it is possible to change semiconductor conductivity by light which irradiates the semiconductor electrode and governs the photoconductivity; in other words, semiconductor is photosensitively doped [44]. Therefore, in Section 4.3, the calculations are carried out for a range of the semiconductor conductivity.

In the Section 4.2 and 4.3, the parameters used for the analysis are presented in the nondimensionalized form. The dimensional analysis for Model-1 can be done easily, which is done in the Reference [45], [46], [47], [48], and [21] because Model-1 only involves Townsend ionization and secondary electron emission as a charged particle source and does not involve energy balance equation. However, it is not applicable for Model-2 and Model-3 since the energy balance equation and the source terms, responsible for more complex interactions given in Table 2.1, cannot be addressed easily.

The question is that how can the results of Model-2 and Model-3 be represented in the dimensionless forms? The answer is the following. The dimensionless coordinates and fields for Model-1 are (taken from Reference [21])

$$\begin{gathered} \mathtt{x} = \frac{x}{X_0}, \quad \tau = \frac{t}{t_0}, \quad \sigma(\mathtt{x}, \tau) = \frac{n_e(x,t)}{n_0} \\ \varepsilon(\mathtt{x}, \tau) = \frac{E(x,t)}{E_0}, \quad \mathtt{U} = \frac{U}{E_0 X_0}, \quad j = \frac{J}{e n_0 X_0 / t_0} \end{gathered} \tag{4.8}$$

for discharge gap, and

$$\tau_s = \frac{T_s}{t_0}, \quad \mathtt{R}_s = \frac{R_s}{E_0 t_0 / e n_0} \tag{4.9}$$

for the semiconductor. X_0, t_0, n_0 and E_0 are scale factors which make the dimensional parameters dimensionless. These factors can be written in terms of dimensional parameters as following

$$X_0 = \frac{1}{\alpha_0}, \quad t_0 = \frac{1}{\alpha_0 \mu_e E_0}, \quad n_0 = \frac{\epsilon_0 \alpha_0 E_0}{e} \tag{4.10}$$

where α_0 is constant for Townsend coefficient given in Table 3.1. Then corresponding values for these intrinsic parameters are calculated as

$$\begin{aligned} X_0 &\approx 2.78 \times 10^{-5} m, \quad t_0 \approx 4.0486 \times 10^{-11} s \\ n_0 &\approx 2.0475 \times 10^{18} m^{-3}, \quad E_0 \approx 1.03 \times 10^{6} V/m \end{aligned} \tag{4.11}$$

The necessary scalings of the results in the following sections are based on the nondimensionalizing of parameters U, U_t, J, t and R_s. By using relations (4.8), (4.9) and scales (4.11), the dimensionless forms of potential, current density, time and electrical resistance can be obtained by dividing them with 28.634 V, 2.2526×10^5 A/m^2, 4.0486×10^{-11} s and 1.2712×10^{-4} Ω, respectively. Thus, the modelling results are indicated by the dimensionless parameters $\mathtt{U}$, $\mathtt{U}_t$, j, τ and $\mathtt{R}_s$ characterizing the gas discharge layer and the semiconductor layer.

4.2 Qualitative features of numerical solutions: stable and unstable solutions

In this section, the qualitative behaviour of the numerical solutions obtained from the models of the gas discharge system coupled with semiconductor layer are investigated. The calculations are made in the subnormal regime because oscillations are observed in the regime between Townsend and glow discharge [20]. The resistance of the semiconductor is taken as $\mathtt{R}_s = 491661.4$, or 62.5 Ωm^2 which corresponds to $\sigma_s = 2.4 \times 10^{-7}$ $(\Omega cm)^{-1}$. When the steady-state condition is considered for the external circuit equation (4.7), the relation $U = U_t - R_s J$ is obtained. The corresponding dimensionless form of this relation is $\mathtt{U} = \mathtt{U}_t - \mathtt{R}_s j$. This is called the load line. Since the load line represents the stationary form of the external circuit, it is related to the stationary solutions of the coupled system. Indeed, the intersection point between the load line and the current-voltage characteristics curve in the phase space $(j, \mathtt{U})$ indicates the stationary solution of the discharge system. In this way, the stationary solutions of each of the models are determined and used as reference points for the qualitative investigations: whether the solutions, which initiate nearly from the equilibrium state, return back to this state or grow to a limit cycle.

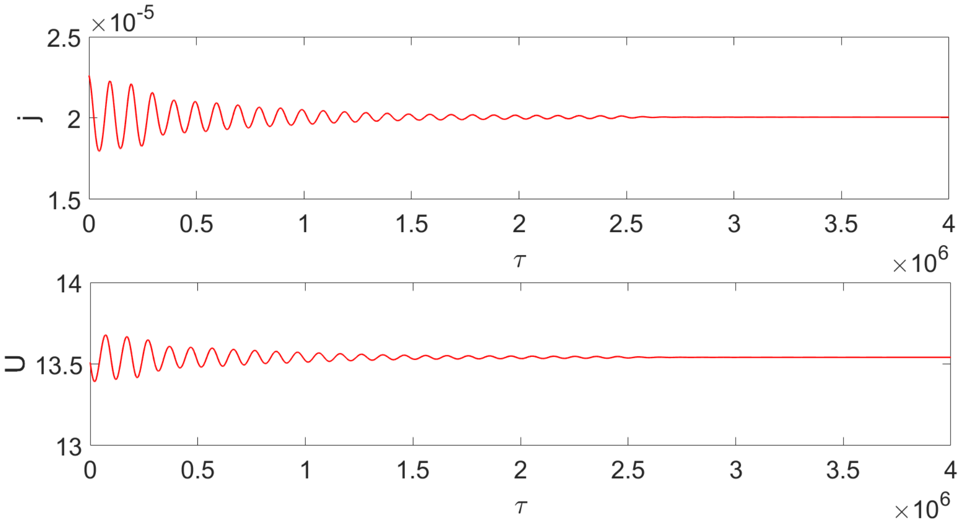

Figure 4.2: $j(\tau)$ and $\mathtt{U}(\tau)$ for Model-1 with $\mathtt{R}_s = 491661, 4$ and $\mathtt{U}_t = 23.16$

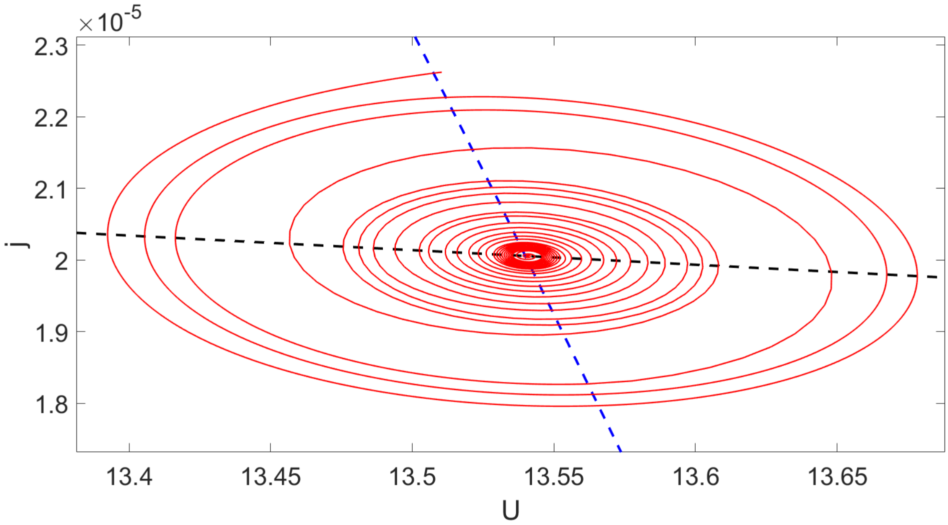

Figure 4.3: Phase space plot of the data from Figure 4.2 with current-voltage characteristics $\mathtt{U} = \mathtt{U}(j)$ and load line $\mathtt{U} = \mathtt{U}_t - \mathtt{R}_s j$

When the calculations by Model-1 are started with the initial condition $(j_0, \mathtt{U}_0) = (2.25 \times 10^{-5}, 13.51)$ with $\mathtt{U}_t = 23.16$, the current density and discharge voltage converge to a fixed point, which is shown in Figure 4.2. This means that the solution is stable. Figure 4.3 shows the phase space plot of data from Figure 4.2. It must be noted that Figure 4.3 contains two additional lines; blue dashed curve is current-voltage characteristics of the gas discharge $\mathtt{U} = \mathtt{U}(j)$, and blacked dashed line is the load line $\mathtt{U} = \mathtt{U}_t - \mathtt{R}_s j$. As it is mentioned before, their intersection indicates the stationary solution of the system; therefore, the perturbated system spirals inwards towards the intersection point, namely equilibrium point.

Since above parameter regime occurs somewhere near the border separating stable from unstable plasma about a bifurcation curve, the solution becomes sensitive to perturbation from the equilibrium state. When the calculations for Model-1 is started with $\mathtt{U}_t = 25.58$, the current density and discharge voltage become unstable and develop into a limit cycle oscillations. This means that the solution becomes dynamically unstable, which is shown in Figure 4.4 and corresponding phase space plot is given in Figure 4.5.

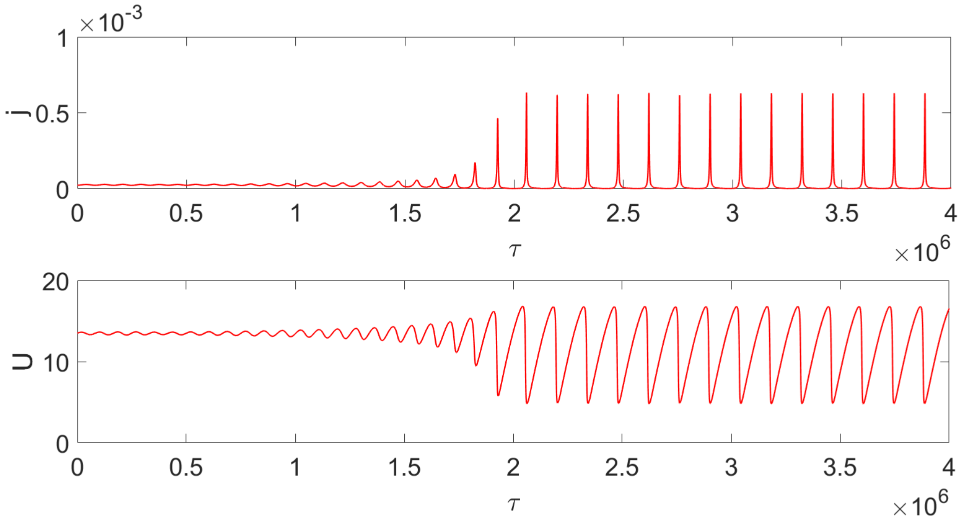

Figure 4.4: $j(\tau)$ and $\mathtt{U}(\tau)$ for Model-1 with $\mathtt{R}_s = 491661.4$ and $\mathtt{U}_t = 25.58$

Unlike the peak currents of Figure 4.5 exploring the subnormal glow regime, the low current regime is close to the Townsend limit since it is located at the turning part of $\mathtt{U}(j)$ representing the transition from subnormal to Townsend regime.

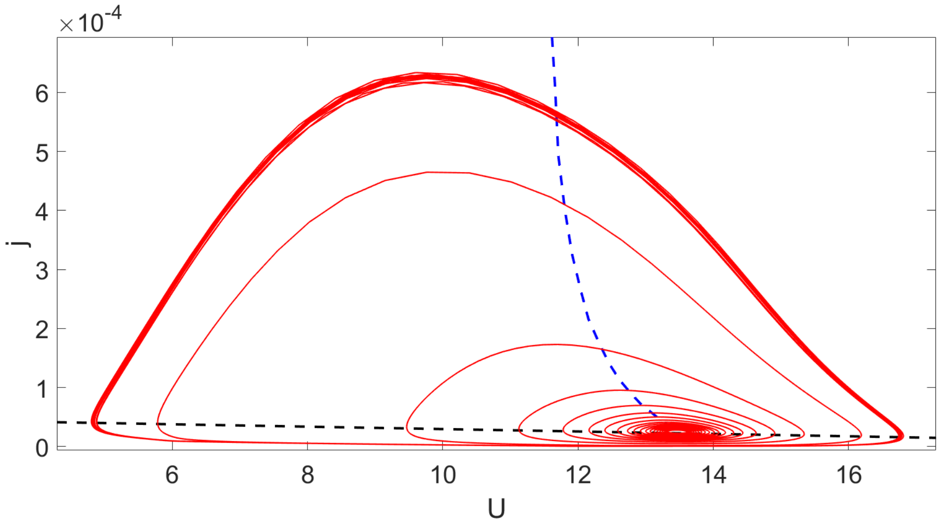

Figure 4.5: Phase space plot of the data from Figure 4.4 with current-voltage characteristics $\mathtt{U} = \mathtt{U}(j)$ and load line $\mathtt{U} = \mathtt{U}_t - \mathtt{R}_s j$

The same analyses can be done for Model-2 and Model-3 in order to qualitatively investigate the response of the stationary discharge to a small perturbation.

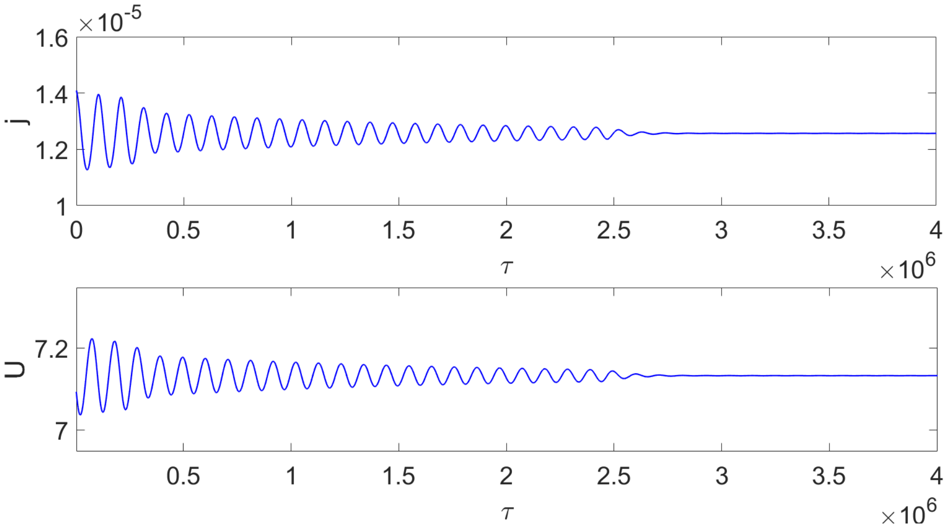

Figure 4.6: $j(\tau)$ and $\mathtt{U}(\tau)$ for Model-2 with $\mathtt{R}_s = 491661.4$ and $\mathtt{U}_t = 13.33$

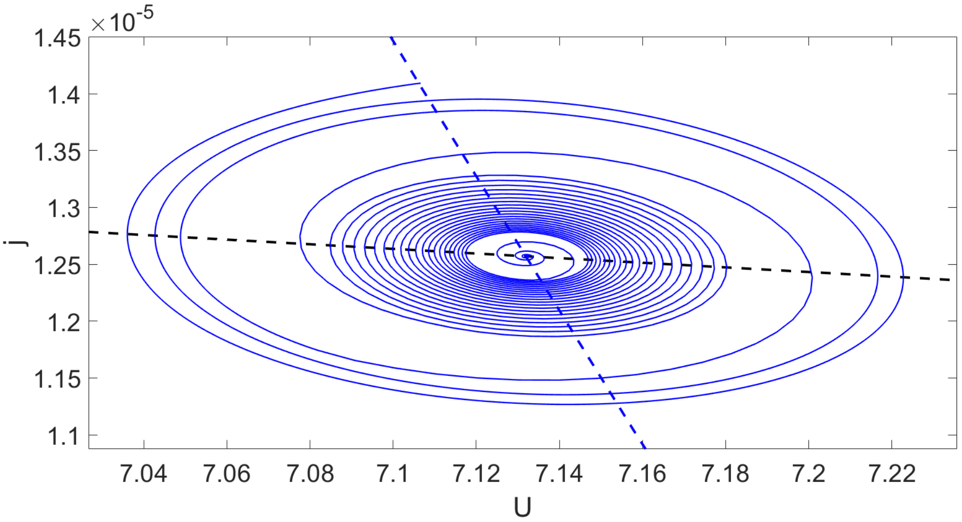

Figure 4.7: Phase space plot of the data from Figure 4.6 with current-voltage characteristics $\mathtt{U} = \mathtt{U}(j)$ and load line $\mathtt{U} = \mathtt{U}_t - \mathtt{R}_s j$

If the initial conditions for Model-2 are chosen as $(j_0, \mathtt{U}_0) = (1.41 \times 10^{-5}, 7.11)$ with $\mathtt{U}_t = 13.33$, then the current density and discharge voltage with respect to time are shown in Figure 4.6. The corresponding phase space plot is depicted in Figure 4.7. When the calculations are initiated at $\mathtt{U}_t = 14.74$, the plots for current density and discharge voltage are illustrated in Figure 4.8. The corresponding phase space plot of data from Figure 4.8 is shown in Figure 4.9.

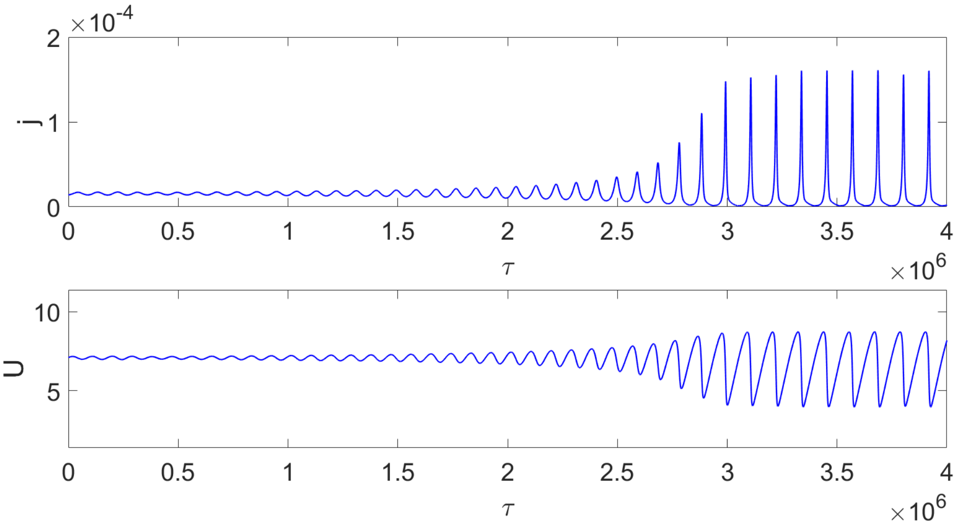

Figure 4.8: $j(\tau)$ and $\mathtt{U}(\tau)$ for Model-2 with $\mathtt{R}_s = 491661.4$ and $\mathtt{U}_t = 14.74$

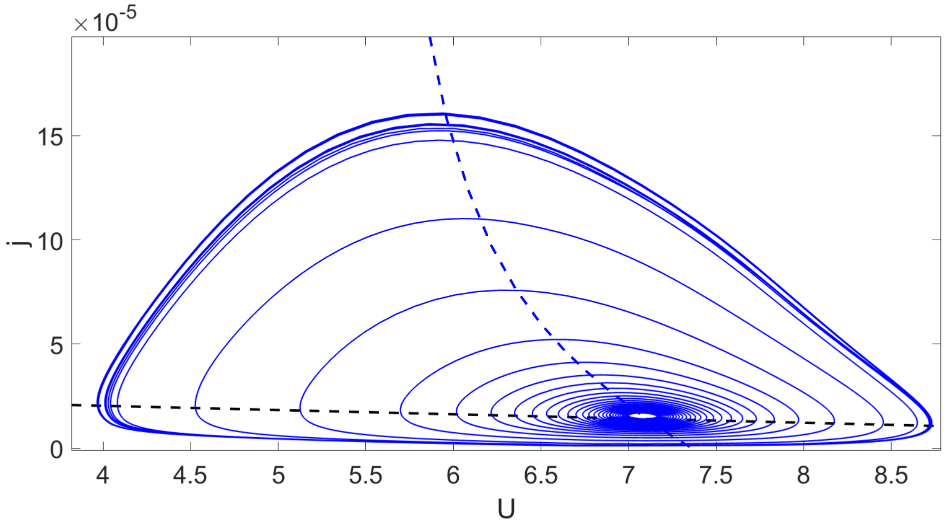

Figure 4.9: Phase space plot of the data from Figure 4.8 with current-voltage characteristics $\mathtt{U} = \mathtt{U}(j)$ and load line $\mathtt{U} = \mathtt{U}_t - \mathtt{R}_s j$

The similar plots can be obtained for Model-3 with different initial conditions and $\mathtt{U}_t$. If the initial condition for Model-3 is taken as $(j_0, \mathtt{U}_0) = (1.59 \times 10^{-5}, 9.70)$ with $\mathtt{U}_t = 16.63$, then $j(\tau)$ and $\mathtt{U}(\tau)$ and corresponding phase portrait are illustrated in Figure 4.10 and Figure 4.11, respectively.

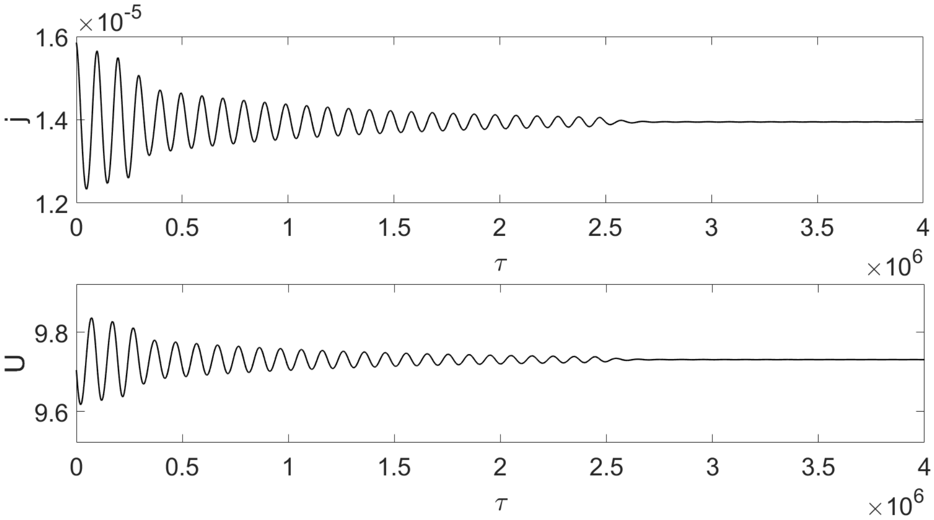

Figure 4.10: $j(\tau)$ and $\mathtt{U}(\tau)$ for Model-3 with $\mathtt{R}_s = 491661.4$ and $\mathtt{U}_t = 16.63$

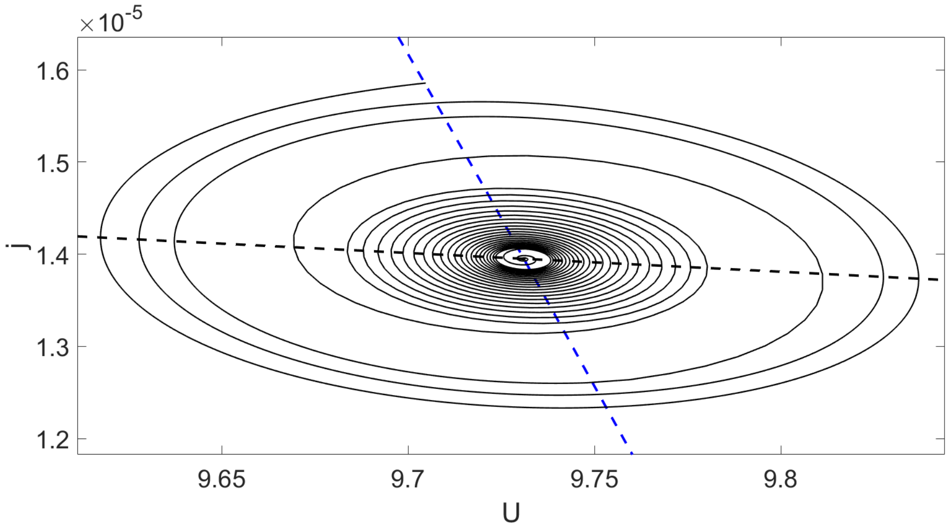

Figure 4.11: Phase space plot of the data from Figure 4.10 with current-voltage characteristics $\mathtt{U} = \mathtt{U}(j)$ and load line $\mathtt{U} = \mathtt{U}_t - \mathtt{R}_s j$

When the calculation for Model-3 is carried out for $\mathtt{U}_t = 18.38$, the current density, voltage and phase space plot are illustrated in Figure 4.12 and Figure 4.13, respectively.

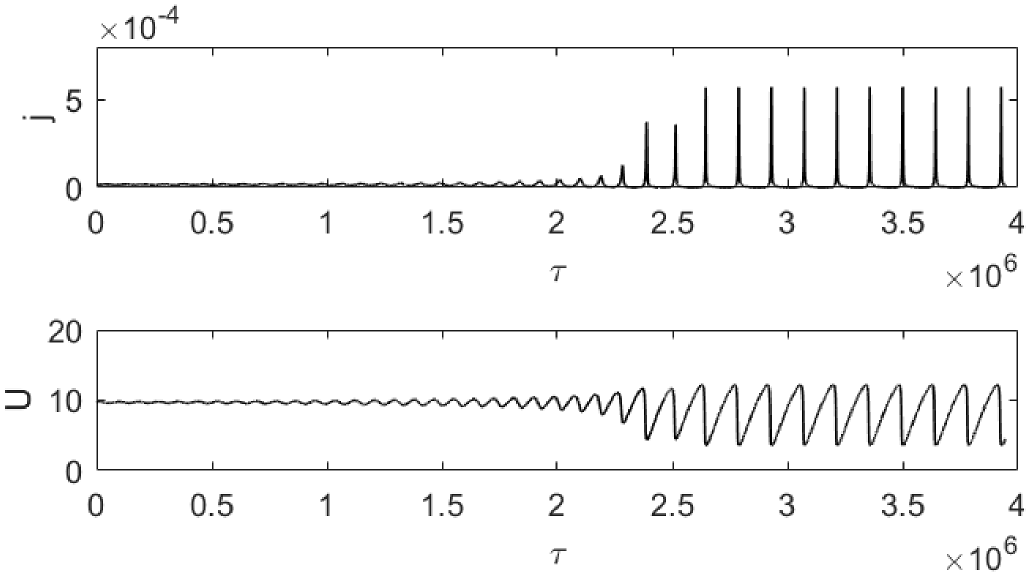

Figure 4.12: $j(\tau)$ and $\mathtt{U}(\tau)$ for Model-3 with $\mathtt{R}_s = 491661.4$ and $\mathtt{U}_t = 18.38$

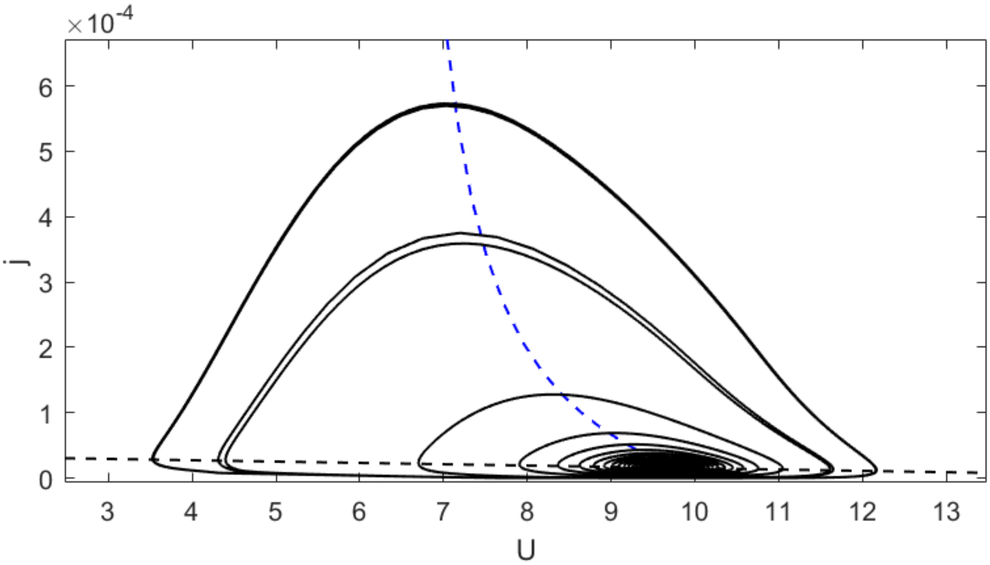

Figure 4.13: Phase space plot of the data from Figure 4.12 with current-voltage characteristics $\mathtt{U} = \mathtt{U}(j)$ and load line $\mathtt{U} = \mathtt{U}_t - \mathtt{R}_s j$

It is seen that the small perturbation from the stationary solution lead to either stability or destability, and this is true for each of the models. This means that there must exist $(\mathtt{U}_t)_{critical}$, called a bifurcation point, indicating the transition from a stable to an unstable solution. Naturally, this value for each of the models can be seeked between values of $\mathtt{U}_t$ corresponding to stable and unstable solutions. In other words, critical value must be found between $\mathtt{U}_t = 23.16$ and $\mathtt{U}_t = 25.58$ for Model-1, $\mathtt{U}_t = 13.33$ and $\mathtt{U}_t = 14.74$ for Model-2, $\mathtt{U}_t = 16.63$ and $\mathtt{U}_t = 18.38$ for Model-3. It is also noted that the calculations for this section only done for $\mathtt{R}_s = 491661.4$, or 62.5 Ωm^2 in the dimensional unit; however, the calculations for different $\mathtt{R}_s$ values for each of the models are necessary to develop a bifurcation diagram, which is done in Section 4.3.

4.3 Deriving the bifurcation curves

As it is mentioned in Section 4.2, when the control parameter $\mathtt{U}_t$ is changed from the value corresponding to a stationary state, the solution either converges to a fixed point or loses its stability with limit cycle oscillations. In section 4.2, the calculations are made for a specific semiconductor resistance ($R_s = 62.5\ \Omega m^2$), and it is concluded that there must be a critical value $(\mathtt{U}_t)_{critical}$ symbolizing the transition from a stable to an unstable solution. This critical point is called bifurcation point since the qualitative changes in the dynamics occur at this point [49]. In this section, the same procedure as in Section 4.2 is applied not only to a specific R_s, but also each R_s value in the range of $32.609\Omega m^2 \leq R_s \leq 1500\Omega m^2$, or $256508.5 \leq \mathtt{R}_s \leq 11800200$ in the dimensionless form. The corresponding bifurcation points for each R_s are investigated to construct a bifurcation curve for each model. These curves give an opportunity to make a comparison with experimental data [27], [28], and [21]. The bifurcation diagram is illustrated in Figure 4.14. The vertical and horizontal axes are specified as $1/\mathtt{R}_s$, conductivity, and $\mathtt{U}_t$, total applied voltage, respectively.

The calculations are made between $1.695 \times 10^{-8} \leq 1/\mathtt{R}_s \leq 3.898 \times 10^{-6}$. In detail, the right hand side of each computed curve exhibits the region in the parameter space where the equilibrium state is unstable and hence the plasma is oscillatory unlike the left hand side indicating the region where equilibrium state is stable. This means that one can predict the equilibrium feature of any solution from the bifurcation diagram given in Figure 4.14 for a specific value of $\mathtt{U}_t$ and $1/\mathtt{R}_s$.

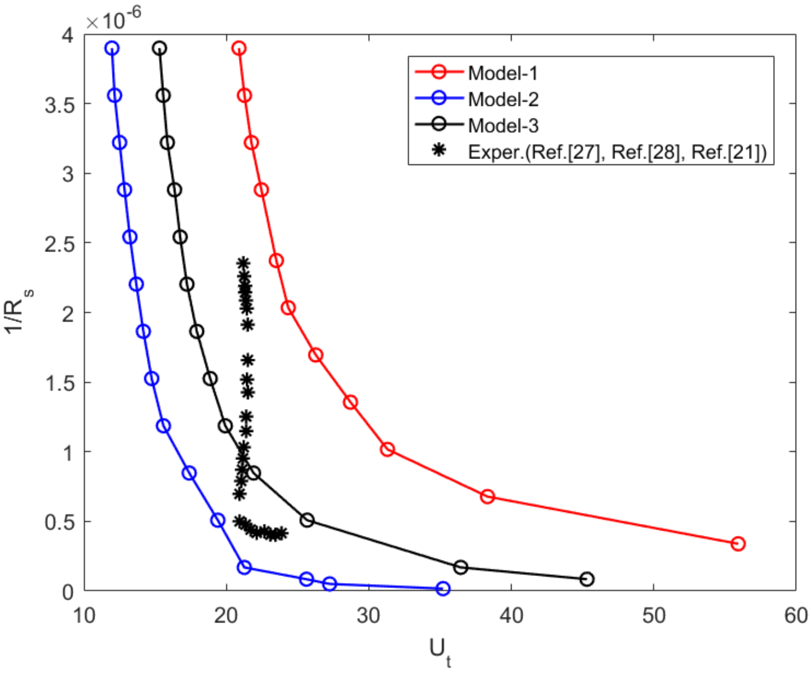

Figure 4.14: Bifurcation diagram: Circles indicate bifurcation curves derived from Model-1, Model-2, Model-3, and stars indicate the experimental data [27], [28], and [21]

When the experimental data is interpreted, the bifurcation line, where the value $1/\mathtt{R}_s$ is larger than 0.5×10^{-6}, initially increases with positive slope then it becomes parallel to the σ_s axis, and later it raises with negative slope up to the end of experimentally reached maximum σ_s value. However, the experimental data for the low conductivity of semiconductor ($1/\mathtt{R}_s \leq 0.5 \times 10^{-6}$) is almost parallel to the $\mathtt{U}_t$ axis. It is noted that the computed bifurcation curves qualitatively fit the experimental curve. However, two lines forming experimental data have quite distinct slope. Unlike this, the theoretical curves obtained from the models change gradually with a continuous slope. Meanwhile, the bifurcation curve obtained from Model-3 depicted with a black curve is the most compatible one with the experimental data. This result is expected because the Model-3 includes more detailed set of chemical reactions than Model-1 and Model-2 as it is stated in Chapter 2. Therefore, Model-3 reflects the physical reality more properly than Model-1 and Model-2.

In this bifurcation diagram, it is seen that a point corresponding to stable solution becomes unstable when control parameter $\mathtt{U}_t$ is increased for a specific $1/\mathtt{R}_s$ value. This is the signature of Hopf bifurcation. In the reference [49], when the value of control parameter is very close to the critical value, the decaying to the stationary solution becomes slower and slower. In our case, Figure 4.2, Figure 4.6 and Figure 4.10 support this argument since $\mathtt{U}_t$ value for each model is taken as 5% smaller than corresponding $(\mathtt{U}_t)_{critical}$, or bifurcation point. If the control parameter increases a little bit more than critical value, then stable equilibrium state will lose its stability and be surrounded by limit cycle oscillations. In our case, Figure 4.4, Figure 4.8 and Figure 4.12 show the similar properties since $\mathtt{U}_t$ value for each model is taken about 5% bigger than corresponding $(\mathtt{U}_t)_{critical}$. Apart from these, when the calculations are started with $\mathtt{U}_t > (\mathtt{U}_t)_{critical}$ and later the value of $\mathtt{U}_t$ is decreased, the solution settles down back to a stable solution, and the results of these calculations do not show any hysteresis. In other words, the amplitude of limit cycle oscillations for each of the considered models shrinks back to zero as the control parameter $\mathtt{U}_t$ is reversed [49]. Because of this, the type of Hopf bifurcation for each model is supercritical Hopf bifurcation.

In conclusion, in this chapter, each of the three considered models is coupled to a semiconductor layer. In Section 4.2, it is seen that the current density and the discharge voltage for each model show temporal changes in the subnormal regime. Either a stable or an unstable equilibrium is observed when the calculation is initiated nearly from the stationary solution. Later, in Section 4.3, supercritical Hopf bifurcation curve for each model is obtained to make a comparison with the experimental data [27], [28], and [21]. It is observed that Model-3 is the most compatible curve to the experimental result. This is expected because Model-3 is more detailed than Model-2, Model-1 in terms of the set of chemical reactions it includes.

CHAPTER 5

CONCLUSION

Three one dimensional discharge models are developed for nitrogen gas by using COMSOL Multiphysics software. Model-1 is based on "simple fluid approach" while Model-2, Model-3 are based on "extended fluid approach". Unlike Model-1 in which transport and rate coefficients are defined as functions of local electric field, called LFA, the transport and rate coefficients of electrons for Model-2 and Model-3 are defined as functions of local electron mean energy, which is called LMEA. Beside, Model-3 is more precise than Model-2 since this model uses more detailed set of plasma chemical reactions. Hence, Model-3 gives more correct estimates than Model-2. Model-2 and Model-3 lead to qualitatively more proper results than Model-1 because the nonlocal transport of electrons is incorporated into these models to some extent by adding an extra energy balance equation.

Chapter 3 tests applicability of these three considered models by comparing CVC curves obtained from the models with measured CVC's available from literature [23], [24], [25], and [26]. It is seen that computed CVC curves from the models show the similar qualitative behaviour with the experimental curves taken from the literature. In detail, CVC curve from Model-3 is the closest one to the experiments. Furthermore, the spatial distributions of basic plasma parameters for each of the models are investigated. It is shown that the discharge characteristics for each of the models computed at three typical DC regimes (abnormal, normal, and subnormal) are consistent to typical plasma discharge behaviour. The main result from this chapter is that three considered models are physically applicable for the following analysis.

After verifications of the models are made, each of the three considered models is coupled to a semiconductor layer at the cathode. It is seen that there are oscillations of plasma parameters (current density and discharge voltage) in the regime between the Townsend and normal glow, and they are classified as stable or unstable as a result of a small perturbation from the stationary state. Later, the critical values, in terms of semiconductor conductivity and applied total voltage, in transition from the stable to unstable solutions are determined to construct bifurcation curves for each of the considered models. The resulting bifurcation curves are compared with experimental data [27], [28], and [21]. It is seen that the computed curves are qualitatively in agreement with experimental data. Moreover, Model-3 provides better qualitative consistency. Thus, this study allows to determine the accuracy and the ranges of applicability of different modelling approaches to understand the temporal oscillations in nonlinear discharge system coupled with a semiconductor layer.

REFERENCES

[1] Umran S. Inan and Marek Golkowski. *Principles of Plasma Physics for Engineers and Scientists.* Cambridge University Press, 2011.

[2] V. Krishan. *Plasmas: the first state of matter.* Cambridge University Press, 2014.

[3] A. I. Morozov. *Introduction to Plasma Dynamics.* CRC Press, 2013.

[4] Michael A. Lieberman and Allan J. Lichtenberg. *Principles of Plasma Discharges and Materials Processing.* John Wiley & Sons, 2005.

[5] Contemporary physics education project. `http://www.cpepphysics.org/fusion_samples.html`.

[6] Yuri P. Raizer. *Gas Discharge Physics.* Springer, 2001.

[7] J. Reece Roth. *Industrial Plasma Engineering Volume 1: Principles.* Institute of Physics Publishing Bristol and Philadelphia, 2001.

[8] F. Paschen. Ueber die zum Funkenübergang in Luft, Wasserstoff und Kohlensäure bei verschiedenen Drucken erforderliche Potentialdifferenz. *Annalen der Physik*, 274:69–96, 1889.

[9] H Bruining. *Physics and applications of secondary electron emission.* London Pergamon Press Ltd, 1962.

[10] Francis F. Chen and Jane P Chang. *Lecture Notes on Principles of Plasma Processing.* Springer, 2003.

[11] Jayr de Amorim Filho. *Gas Discharges - Fundamentals & Applications.* Transworld Research Network, 2007.

[12] G. K. Grubert, M. M. Becker, and D. Loffhagen. Why the local-mean-energy approximation should be used in hydrodynamic plasma descriptions instead of the local-field approximation. *Physical Review E*, 80:036405, 2009.

[13] Vladimir Kolobov and Robert Arslanbekov. Deterministic Boltzmann solver for electron kinetics in plasma reactors for microelectronics applications. *Microelectronic Engineering*, 69:606–615, 2003.

[14] J. P. Trelles. Pattern Formation and self-organization in plasmas interacting with surfaces. *Journal of Physics D: Applied Physics*, 49:393002, 2016.

[15] M. C. Cross and P. C. Hohenberg. Pattern formation outside of equilibrium. *Reviews of Modern Physics*, 65:851–1111, 1993.

[16] Pattern formation in planar dc gas-discharge systems. `https://www.uni-muenster.de/Physik.AP/Purwins/DC/index-en.html`.

[17] H. G. Purwins and L. Stollenwerk. Synergetic aspects of gas-discharge: lateral patterns in dc systems with a high ohmic barrier. *Plasma Physics and Controlled Fusion*, 56:123001, 2014.

[18] H. Willebrand, T. Hünteler, F. J. Niedernostheide, R. Dohmen, and H. G. Purwins. Periodic and turbulent behavior of solitary structures in distributed active media. *Physical Review A*, 45:8766–8775, 1991.

[19] C. Strümpel, Yu. A. Astrov, and H. G. Purwins. Multioscillatory patterns in a hybrid semiconductor gas discharge system. *Physical Review E*, 65:066210, 2002.

[20] C. Strümpel, Yu. A. Astrov, and H. G. Purwins. Nonlinear interaction of homogeneously oscillating domains in a planar gas discharge system. *Physical Review E*, 62:4889–4897, 2000.

[21] D. D. Sijacic, U. Ebert, and I. Rafatov. Oscillations in dc driven barrier discharge: Numerical solutions, stability analysis, and phase diagram. *Physical Review E*, 71:066402, 2005.

[22] COMSOL MULTIPHYSICS 5.2. `https://www.comsol.com/`.

[23] S. Gocic, N. Skoro, D. Maric, and Z. Lj. Petrovic. Influence of the cathode surface conditions on V-A characteristics in low-pressure nitrogen discharge. *Plasma Sources Science and Technology*, 23:035003, 2014.

[24] M. M. Monsour, N. M. El-Sayed, O. F. Farag, and M. H. Elghazaly. Effect of He and Ar Addition on N_2 Glow Discharge Characteristics and Plasma Diagnotics. *Arab Journal of Nuclear Science and Applications*, 46:116–125, 2013.

[25] M. A. Hassouba and E. A. Mehanna. Electrical characteristics of (N_2-H_2) gas mixture DC glow discharge. *International Journal of Physical Sciences*, 4:713–721, 2009.

[26] K. Takaki, M. Hosokawa, T. Sakaki, Mukaigawa, and T. Fujiwara. Voltage-Current Characteristics of Nitrogen High-Current Glow Discharge. *Journal of Advanced Oxidation Technologies*, 8:11–17, 2005.

[27] C. Strümpel. Ph.D. thesis, University of Münster. 2001.

[28] D. Sijacic. Ph.D. thesis, Technical University of Eindhoven. 2004.

[29] F. F. Chen. *Introduction to plasma physics and controlled fusion.* Springer, 2015.

[30] D. J. Griffiths. *Introduction to electrodynamics.* Cambridge University Press, 2017.

[31] Sergey T. Surzhikov and Joseph S. Shang. Two-component plasma model for two-dimensional glow discharge in magnetic field. *Journal of Computational Physics*, 199:437–464, 2004.

[32] S. Surzhikov and J. Shang. Normal glow discharge in axial magnetic field. *Plasma Sources Science and Technology*, 23:054017, 2014.

[33] I. Rafatov, E. A. Bogdanov, and A. A. Kudryavtsev. On the accuracy and reliability of different fluid models of the direct current glow discharge. *Physics of Plasmas*, 19:03352, 2012.

[34] B. Chapman. *Glow Discharge Processes Sputtering and Plasma Etching.* John Wiley & Sons, 1980.

[35] G. J. M. Hagelaar and L. C. Pitchford. Solving the Boltzmann equation to obtain electron transport coefficients and rate coefficients for fluid models. *Plasma Sources Sci. Technol.*, 14:722–733, 2005.

[36] Phelps and pitchford. `http://www.lxcat.net`.

[37] Y. H. Choi, J. H. Kim, and Y. S. Hwang. One-dimensional discharge simulation of nitrogen DBD atmospheric pressure plasma. *Thin Solid Films*, 506-507:389–395, 2006.

[38] F. Tochikubo, S. Uchida, H. Yasui, and K. Sato. Numerical Solution of NO Oxidation in Dielectric Barrier Discharge with Microdischarge Formation. *Japanese Journal of Applied Physics*, 48:076507, 2009.

[39] M. Capitelli, M. Ferreira, F. Gordiets, and A. I. Osipov. *Plasma Kinetics in Athmospheric Gases.* Springer, 2000.

[40] J. P. Boeuf and L. C. Pitchford. Two-dimensional model of a capacitively coupled rf discharge and comparisons with experiments in the Gaseous Electronics Conference reference reactor. *Physical Review E*, 51:1376–1390, 1995.

[41] G. J. M. Hagelaar, F. J. deHoog, and G. M. W Kroesen. Boundary conditions in fluid models of gas discharges. *Physical Review E*, 62:1452–1454, 2000.

[42] Mumps. `http://mumps.enseeiht.fr/`.

[43] *Introduction to COMSOL Multiphysics 5.2.* COMSOL, 2015.

[44] E. Ammelt, Yuri P. Raizer, and H. G. Purwins. Hexagon structures in a two-dimensional dc-driven gas discharge systems. *Physical Review E*, 58:7109–7117, 1998.

[45] D. D. Sijacic, U. Ebert, and I. Rafatov. Period doubling cascade in glow discharge: Local versus global differential conductivity. *Physical Review E*, 70:056220, 2004.

[46] D. D. Sijacic and U. Ebert. Transition from Townsend to glow discharge: Subcritical, mixed, or supercritical characteristics. *Physical Review E*, 66:066410, 2002.

[47] Yuri P. Raizer, U. Ebert, and D. D. Sijacic. Dependence of the transition from Townsend to glow discharge on secondary emission. *Physical Review E*, 70:017401, 2004.

[48] U. Ebert, Wim van Saarloos, and Christiane Caroli. Propagation and structure of planar streamer fronts. *Physical Review E*, 55:1530–1549, 1997.

[49] S. H. Strogatz. *Nonlinear Dynamics and Chaos: With Applications to Physics, Biology, Chemistry and Engineering (Studies in Nonlinearity)*. Westview Press, 2015.